

# SIimulator of GALaxy Millimeter/submillimeter Emission (SÍGAME<sup>\*</sup>): CO emission from massive $z = 2$ main sequence galaxies

Karen P. Olsen<sup>1†</sup>, Thomas R. Greve,<sup>2</sup> Christian Brinch,<sup>3,4</sup> Jesper Sommer-Larsen,<sup>1,5,6</sup> Jesper Rasmussen,<sup>1,7</sup> Sune Toft,<sup>1</sup> Andrew Zirm<sup>1</sup>

<sup>1</sup>*Dark Cosmology Centre, Niels Bohr Institute, University of Copenhagen, Juliane Maries Vej 30, DK-2100 Copenhagen, Denmark*

<sup>2</sup>*Dept. Physics and Astronomy, University College London*

<sup>3</sup>*Centre for Star and Planet Formation (Starplan) and Niels Bohr Institute, University of Copenhagen, Juliane Maries Vej 30, DK-2100 Copenhagen, Denmark*

<sup>4</sup>*DeIC, Technical University of Denmark, Building 309, DK-2800 Kgs. Lyngby, Denmark*

<sup>5</sup>*Excellence Cluster Universe, Boltzmannstr. 2, 85748 Garching, Germany*

<sup>6</sup>*Marie Kruses Skole, Stavnsholtvej 29-31, DK-3520 Farum, Denmark*

<sup>7</sup>*Department of Physics, Technical University of Denmark, Building 309, DK-2800 Kgs. Lyngby, Denmark*

## ABSTRACT

We present SÍGAME (SIimulator of GALaxy Molecular Emission), a new numerical code designed to simulate the  $^{12}\text{CO}$  rotational line emission spectrum of galaxies. Using sub-grid physics recipes to post-process the outputs of smoothed particle hydrodynamics (SPH) simulations, a molecular gas phase is condensed out of the initial hot and partly ionised SPH gas and distributed in Giant Molecular Cloud (GMCs). The GMCs are subjected to far-UV radiation fields and cosmic ray ionisation rates which scale with the local star formation rate volume density, thereby ensuring that the thermal state of the gas is directly coupled to the in situ star formation conditions. Level populations as well as line radiative transport of the CO rotational lines are solved for with the 3-D radiative transfer code LIME. We have applied SÍGAME to cosmological SPH simulations of three disk galaxies at  $z = 2$  with stellar masses in the range  $\sim 0.5 - 2 \times 10^{11} M_{\odot}$  and star formation rates  $\sim 40 - 140 M_{\odot} \text{ yr}^{-1}$ , for which we predict a low-excitation gas with CO intensity peaks at the CO  $J = 3 - 2$  transition and total CO( $3 - 2$ ) luminosities within the range of observations of corresponding star-forming galaxies at  $z \sim 1 - 2.5$ . Global  $\alpha_{\text{CO}}$  factors range from 1.4 to  $1.6 M_{\odot} \text{ pc}^{-2} (\text{K km s}^{-1})^{-1}$ , i.e. about a third of the Galactic value. On resolved scales, the model galaxies display an increase in CO( $J - (J - 1)$ )/CO( $1 - 0$ ) brightness temperature line ratios at  $J \geq 3$ , but a decrease in  $\alpha_{\text{CO}}$  towards the central regions, in agreement with observations of nearby galaxies. Adopting a steeper GMC radial density profile or a more shallow mass spectrum leads to increased  $\alpha_{\text{CO}}$  factors, though still below the Galactic value. The inclusion of high pressure ( $P_{\text{ext}}/k_B > 10^4 \text{ K cm}^{-3}$ ) environments decreases line ratios at high- $J$ .

**Key words:** galaxies: high-redshift – galaxies: ISM – ISM: clouds – ISM: lines and bands – methods: numerical – radiative transfer

## 1 INTRODUCTION

Inferring the physical properties of the molecular gas in galaxies is an important prerequisite for understanding their star formation. The rotational lines of the carbon monoxide (CO) molecule has proven to be a valuable tracer of

molecular gas properties, its rotational levels probing a wide range of densities and easily excited by collisions with  $\text{H}_2$  molecules in the interstellar medium (ISM). The CO spectral line energy distribution (SLED) has therefore been used extensively to probe the molecular gas amount of galaxies at high and low redshift (see review by Carilli et al. 2013). With facilities such as the Atacama Large Millimeter Array (ALMA) and the Jansky Very Large Array (JVLA) it is now feasible to observe CO out to  $z \gtrsim 6$ , thus paving the way

<sup>\*</sup> SÍGAME means ‘follow me’ in Spanish.

<sup>†</sup> E-mail: karen@dark-cosmology.dk

for a comprehensive study of how star formation in galaxies depends on their ISM conditions.

An important complement to the observations are galaxy evolution simulations that incorporate a molecular ISM phase and its CO emission properties, as such simulations allow us to interpret and predict the observed molecular emission of galaxies in various evolutionary stages. The past decade saw the development of the first detailed simulations of CO line emission from galaxies. These consisted of SPH galaxy simulations (Narayanan et al. 2006, 2011; Narayanan & Krumholz 2014; Greve & Sommer-Larsen 2008), or semi-analytical models (Obreschkow et al. 2009, 2011; Lagos et al. 2012; Muñoz & Furlanetto 2014; Popping et al. 2014), combined with sub-grid physics prescriptions to model the molecular gas phase and its CO content. The simulations were used to examine the CO emission properties of high- $z$  mergers and starbursts (Narayanan et al. 2008c, 2009), active galactic nuclei (AGN) and quasars (Narayanan et al. 2006, 2008b,a), as well as moderately star-forming galaxies (Greve & Sommer-Larsen 2008; Narayanan et al. 2011; Lagos et al. 2012; Popping et al. 2014). Simulating a large set of disk galaxies, Narayanan & Krumholz (2014) found that the CO SLED can be parameterised with respect to SFR surface density, thus potentially providing a link between a direct observable quantity and the full CO SLED. Simulations of CO line emission has also been related to the underlying total gas mass and SFR for a better understanding of the Kennicutt-Schmidt relation between gas density and SFR, as well as the CO-to-H<sub>2</sub> conversion factor ( $X_{\text{CO}}$ ) relating velocity-integrated CO line intensity to H<sub>2</sub> column density, in low- and high- $z$  galaxies (e.g., Narayanan et al. 2011; Narayanan & Hopkins 2013).

The number of high- $z$  galaxies with well-sampled CO SLEDs, i.e., with multiple CO transitions observed, is still low, and consists mainly of the most luminous objects such as submillimeter galaxies (SMGs) and powerful QSOs. The CO SLEDs of SMGs and QSOs tend to peak the  $J = 5 - 4$  and  $6 - 5$  transitions, suggestive of significant amounts of warm and dense gas. Only a few high- $z$  “main sequence” (MS) galaxies have been observed in multiple CO transitions, and as a result little is known, however, about the ISM conditions of normal star-forming galaxies at high redshifts. The best studied cases are the four BzK-selected galaxies BzK-4171, BzK-16000, and BzK-21000 at  $z \simeq 1.5$ , which have four observed CO transitions, including CO(1-0), (Daddi et al. 2014). Initial analyses of the low- $J$  ( $J_{\text{up}} \leq 3$ ) transitions suggested a quiescent ISM reminiscent of the Milky Way (MW) (Dannerbauer et al. 2009; Aravena et al. 2014). However, recent CO(5-4) observations do not fit with this picture, requiring a second ISM component of high density and possibly high temperature gas, which is thought to be directly associated with star forming clumps within the galaxies (Daddi et al. 2014).

Here we present a new numerical framework for simulating the molecular line emission from star-forming galaxies. The code, Simulator of Galaxy Millimeter/submillimeter Emission (**SÍGAME**), combines (non-)cosmological (SPH or grid-based) simulations of galaxies with subgrid physics prescriptions for the H<sub>2</sub>/HI fraction and thermal balance throughout the ISM, down to parsec scales. **SÍGAME** accounts for a FUV and cosmic ray intensity field that vary with local SFR density within the galaxy. **SÍGAME** can be applied to any

galaxy simulated in the SPH formalism, though currently restricted to galaxies dominated by star formation processes rather than AGN and with mean metallicities above about  $0.01Z_{\odot}$ . Here, we adapt the code to cosmological SPH simulations of three massive, normal star-forming galaxies at  $z = 2$  (i.e., so-called main-sequence galaxies), and model their CO rotational line spectrum using a publicly available 3D radiative transfer code. We show that **SÍGAME** reproduces observed low- $J$  CO line luminosities and provides new estimates of the  $X_{\text{CO}}$  factor for main-sequence galaxies at  $z \sim 2$ , while at the same time predicting their CO line luminosities at high- $J$  ( $J_{\text{up}} > 6$ ) transitions where observations are yet to be made.

The structure of the paper is as follows. Section 2 describes the cosmological SPH simulations used, along with the basic properties of the three star-forming galaxies extracted from the simulations. A detailed description of **SÍGAME** is presented in Section 3. The CO emission maps and spectra obtained after applying **SÍGAME** to the three simulated galaxies are presented in Section 4, where we also compare to actual CO observations of similar galaxies at  $z \sim 2$ . Section 5 discusses the strengths and weaknesses of **SÍGAME** in the context of other molecular line (CO) simulations and recent observations. Finally, in Section 6 we summarise the main steps of **SÍGAME**, and list its main findings and predictions regarding the CO line emission from massive, star-forming galaxies at  $z \simeq 2$ . We adopt a flat cold dark matter ( $\Lambda$ CDM) scenario with  $\Omega_m = 0.3$ ,  $\Omega_{\Lambda} = 0.7$  and  $h = 0.65$ .

## 2 COSMOLOGICAL SIMULATIONS

### 2.1 SPH simulations

We employ a cosmological TreeSPH code for simulating galaxy formation and evolution, though in principle, grid-based hydrodynamic simulations could be incorporated equally well. The TreeSPH code used for the simulations is in most respects similar to the one described in Sommer-Larsen et al. (2005) and Romeo et al. (2006). A cosmic baryon fraction of  $f_b = 0.15$  is assumed, and simulations are initiated at a redshift of  $z = 39$ . The implementation of star formation and stellar feedback, however, has been manifestly changed.

Star formation is assumed to take place in cold gas ( $T_k \lesssim 10^4$  K) at densities  $n_H > 1 \text{ cm}^{-3}$ . The star formation efficiency (or probability that a gas particle will form stars) is formally set to 0.1, but is, due to effects of self-regulation, considerably lower. Star formation takes place in a stochastic way, and in a star formation event, 1 SPH gas particle is converted completely into 1 stellar SPH particle, representing the instantaneous birth of a population of stars according to a Chabrier (2003) stellar initial mass function (IMF; Chabrier (2003)) – see further below.

The implementation of stellar feedback is based on a subgrid super-wind model, somewhat similar to the ‘high-feedback’ models by Stinson et al. (2006). These models, though, build on a supernova blast-wave approach rather than super-wind models. Both types of models invoke a Chabrier (2003) IMF, which is somewhat more top-heavy in terms of energy and heavy-element feedback than, e.g., the standard Salpeter IMF. The present models result in galaxies characterized by reasonable  $z = 0$  cold gas fractions, abundances and circum-galactic medium abundance

properties. They also improve considerably on the “angular momentum problem” relative to the models presented in, e.g., Sommer-Larsen et al. (2003). The models will be described in detail in a forthcoming paper (Sommer-Larsen et al. 2014, in prep.).

## 2.2 The model galaxies

Three model galaxies, hereafter referred to as G1, G2 and G3 in order of increasing SFR, were extracted from the above SPH simulation and re-simulated using the ‘zoom-in’ technique described in (e.g., Sommer-Larsen et al. 2003). The emphasis in this paper is on massive ( $M_* \gtrsim 5 \times 10^{10} M_\odot$ ) galaxies, and the three galaxies analyzed are therefore larger, rescaled versions of galaxies formed in the  $10/h$  Mpc cosmological simulation described in Sommer-Larsen et al. (2003). The linear scale-factor is of the order 1.5, and since the CDM power spectrum is fairly constant over this limited mass range the rescaling is a reasonable approximation.

Galaxy G1 was simulated at fairly high resolution, using a total of  $1.2 \times 10^6$  SPH and dark matter particles, while about  $9 \times 10^5$  and  $1.1 \times 10^6$  particles were used in the simulations of G2 and G3, respectively. For the G1 simulation, the masses of individual SPH gas, stellar and dark matter particles are  $m_{\text{SPH}} = m_* \approx 6.3 \times 10^5 h^{-1} M_\odot$  and  $m_{\text{DM}} = 3.5 \times 10^6 h^{-1} M_\odot$ , respectively. Gravitational (cubic spline) softening lengths of 310, 310 and  $560 h^{-1} \text{pc}$ , respectively, were employed. Minimum gas smoothing lengths were about  $50 h^{-1} \text{pc}$ . For the lower resolution simulations of galaxies G2 and G3, the corresponding particle masses are  $m_{\text{SPH}} = m_* \approx 4.7 \times 10^6 h^{-1} M_\odot$  and  $m_{\text{DM}} = 2.6 \times 10^7 h^{-1} M_\odot$ , respectively, and the gravitational softening lengths were 610, 610 and  $1090 h^{-1} \text{pc}$ . Minimum gas smoothing lengths were about  $100 h^{-1} \text{pc}$ .

Due to effects of gravitational softening, typical velocities in the innermost parts of the galaxies (typically at radii less than about  $2\epsilon_{\text{SPH}}$ , where  $\epsilon_{\text{SPH}}$  is the SPH and star particle gravitational softening length) are somewhat below dynamical values (see, e.g. Sommer-Larsen et al. 1998). The dynamical velocities will be of the order  $v_{\text{dyn}} = \sqrt{GM(R)/R}$ , where  $G$  is the gravitational constant,  $R$  is the radial distance from the centre of the galaxy and  $M(R)$  is the total mass located inside of  $R$ . Indeed, it turns out that for the simulated galaxies considered in this paper SPH particle velocities inside of  $2\epsilon_{\text{SPH}}$  are only about 60-70% of what should be expected from dynamics. To coarsely correct for this adverse numerical effect, for SPH particles inside of  $2\epsilon_{\text{SPH}}$  the velocities are corrected as follows: For SPH particles of total velocity less than  $v_{\text{dyn}}$ , the tangential component of the velocity is increased such that the total velocity becomes equal to  $v_{\text{dyn}}$ . Only the tangential component is increased in order not to create spurious signatures of merging. With this correction implemented, the average ratio of total space velocity to dynamical velocity of all SPH particles inside of  $2\epsilon_{\text{SPH}}$  equals unity.

Figure 1 shows surface density maps of the SPH gas in G1, G2, and G3, i.e., prior to any post-processing by SÍGAME. The gas is seen to be strongly concentrated towards the centre of each galaxy and structured in spiral arms containing clumps of denser gas. The spiral arms reach out to a radius of about 20 kpc in G1 and G3, with G2 showing a

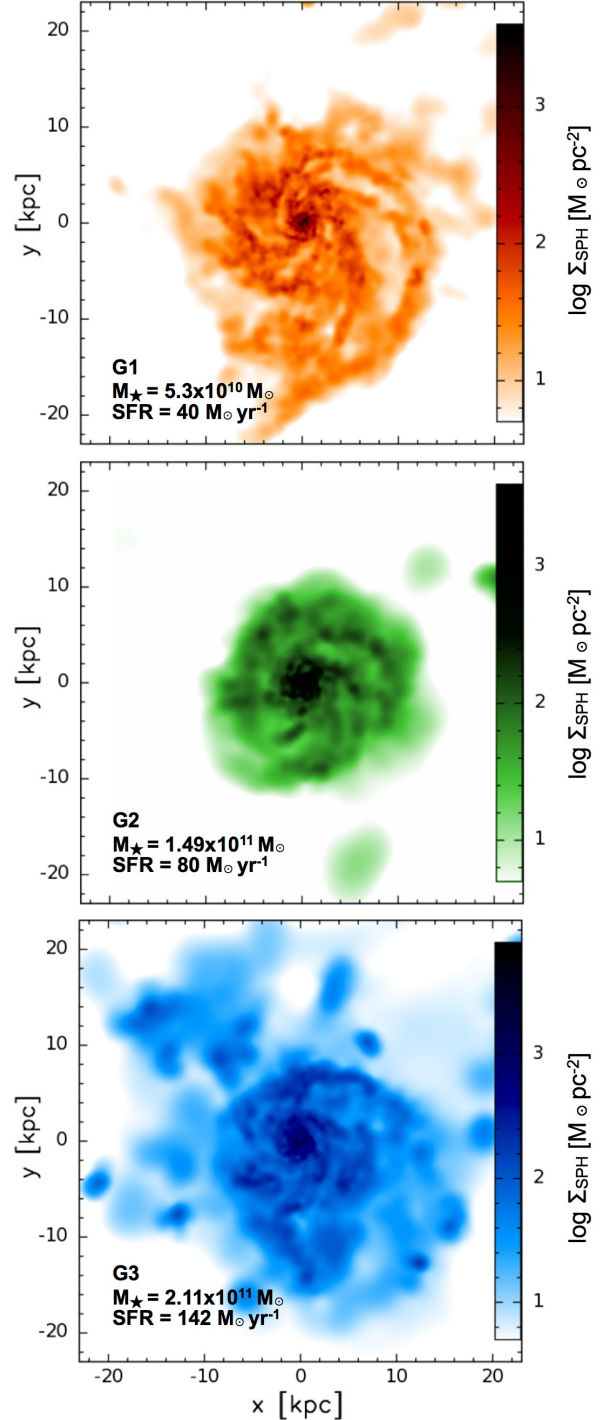


**Figure 1.** SPH gas surface density maps of the three model galaxies G1 (top), G2 (middle), and G3 (bottom) viewed face-on. The stellar masses and SFRs of each galaxy are indicated (see also Table 1). The maps have been rendered with the visualization tool SPLASH version 2.4.0 (Price 2007) using the gas smoothing lengths provided by the simulations.

**Table 1.** Physical properties of the three simulated galaxies G1, G2, and G3

	SFR [ $M_{\odot} \text{ yr}^{-1}$ ]	$M_*$ [ $10^{11} M_{\odot}$ ]	$M_{\text{SPH}}$ [ $10^{10} M_{\odot}$ ]	$f_{\text{SPH}}$	$Z'$	$R_{\text{cut}}$ [kpc]
G1	40	0.53	2.07	29%	1.16	20
G2	80	1.49	2.63	14%	1.97	15
G3	142	2.11	4.66	11%	1.36	20

**Notes.** All quantities are determined within a radius  $R_{\text{cut}}$ , which is the radius where the cumulative radial stellar mass function of each galaxy becomes flat. The gas mass ( $M_{\text{SPH}}$ ) is the total SPH gas mass within  $R_{\text{cut}}$ . The metallicity ( $Z' = Z/Z_{\odot}$ ) is the mean of all SPH gas particles within  $R_{\text{cut}}$ .

more compact structure that does not exceed  $R \sim 15 \text{ kpc}$ . Table 1 lists key properties of these galaxies, namely SFR, stellar mass ( $M_*$ ), SPH gas mass ( $M_{\text{SPH}}$ ), SPH gas mass fraction ( $f_{\text{SPH}} = M_{\text{SPH}}/(M_* + M_{\text{SPH}})$ ), and metallicity  $Z'$ . These quantities were measured within a radius ( $R_{\text{cut}}$ , also given in Table 1) corresponding to where the radial cumulative stellar mass function has flattened out. The metallicity is in units of solar metallicity and is calculated from the abundances of C, N, O, Mg, Si, S, Ca and Fe in the SPH simulations, and adjusted for the fact that not all heavy metals have been included according to the solar element abundances measured by Asplund et al. (2009).

The location of our three model galaxies in the SFR- $M_*$  diagram is shown in Figure 2 along with a sample of 3754  $1.4 < z < 2.5$  main-sequence galaxies selected in near-IR from the NEWFIRM Medium-Band Survey (Whitaker et al. 2011). The latter used a Kroupa IMF but given its similarity with a Chabrier IMF no conversion in the stellar mass and SFR was made (cf., Papovich et al. (2011) and Zahid et al. (2012) who use conversion factors of 1.06 and 1.13, respectively). Also shown are recent determinations of the main-sequence relation at  $z > 1$  (Daddi et al. 2007; Elbaz et al. 2007; Rodighiero et al. 2010). When comparing to the relation at  $z = 2$  of Daddi et al. (2007), G1, G2, and G3 are seen to lie at the massive end of the sequence, albeit somewhat on its lower (i.e., ‘passive’) side. This latter tendency is also found among a subset of CO-detected BX/BM galaxies at  $z \sim 2 - 2.5$  (Tacconi et al. 2013), highlighted in Figure 2 along with a handful of  $z \sim 1.5$  BzK galaxies also detected in CO (Daddi et al. 2010). The BX/BM galaxies are selected by a UGR colour criteria (Adelberger et al. 2004), while the BzK galaxies are selected by the BzK colour criteria (Daddi et al. 2004). Based on the above we conclude that, in terms of stellar mass and SFR, our three model galaxies are representative of the star-forming galaxy population detected in CO at  $z \sim 2$ .

### 3 MODELING THE ISM WITH SÍGAME

#### 3.1 Methodology overview

Here we give an overview of the major steps that go into SÍGAME, along with a brief description of each. The full details of each step are given in subsequent sections and in

appendices A through C. We stress, that SÍGAME operates entirely in the post-processing stage of an SPH simulation, and can in principle easily be adapted to any given SPH galaxy simulation as long as certain basic quantities are known for each SPH particle in the simulation, namely: position ( $\vec{r}$ ), velocity ( $\vec{v}$ ), atomic hydrogen density ( $n_{\text{H}}$ ), metallicity ( $Z'$ ), kinetic temperature ( $T_{\text{k}}$ ), smoothing length ( $h$ ), and star formation rate (SFR). The key steps involved in SÍGAME are:

(i) Cooling of the SPH gas. The initially hot ( $T_{\text{k}} \sim 10^{3-7} \text{ K}$ ) SPH gas particles are cooled to temperatures typical of the warm neutral medium ( $\lesssim 10^4 \text{ K}$ ) by atomic and ionic cooling lines primarily.

(ii) Inference of the molecular gas mass fraction ( $f'_{\text{mol}} = m_{\text{H}_2}/m_{\text{SPH}}$ ) of each SPH particle after the initial cooling in step 1.  $f'_{\text{mol}}$  for a given SPH particle is calculated by taking into account its temperature, metallicity, and the local cosmic ray and FUV radiation field impinging on it.

(iii) Distribution of the molecular gas into GMCs. Cloud masses and sizes are obtained from random sampling of the observed GMC mass-spectrum in nearby quiescent galaxies and applying the local GMC mass-size relation.

(iv) GMC thermal structure. A radial density profile is adopted for each GMC and used to calculate the temperature structure throughout individual clouds, taking into account heating and cooling mechanisms relevant for neutral and molecular gas, when exposed to the local cosmic ray and attenuated FUV fields.

(v) Radiative transport of CO lines. Finally, the CO line spectra are calculated separately for each GMC with a radiative transfer code and accumulated on a common velocity axis for the entire galaxy.

Determining the temperature (step *i*) and the molecular gas mass fraction (step *ii*) of a warm neutral gas SPH particle cannot be done independently of each other, but must be solved for simultaneously in an iterative fashion (see Sections 3.2 and 3.3). As already mentioned, we shall apply SÍGAME to the SPH simulations of galaxies G1, G2, and G3 described in Section 2, and in doing so we will use them to illustrate the workings of the code.

#### 3.2 The Warm and Cold Neutral Medium

In SPH simulations of galaxies the gas is typically not cooled to temperatures below a few thousand Kelvin (Springel & Hernquist 2003). This is illustrated in Figure 3, which shows the SPH gas temperature distribution (dashed histogram) in G1 (for clarity we have not shown the corresponding temperature distributions for G2 and G3, both of which are similar to that of G1). Minimum SPH gas temperatures in G1, G2 and G3 are about 1200 K, 3100 K and 3200 K, respectively, and while temperatures span the range  $\sim 10^{3-7} \text{ K}$ , the bulk ( $\sim 80 - 90\%$ ) of the gas mass in all three galaxies is at  $T_{\text{k}} \lesssim 10^5 \text{ K}$ .

At such temperatures all gas will be in atomic or ionised form and H atoms that attach to grain surfaces via chemical bonds (chemisorbed) will evaporate from dust grains before  $\text{H}_2$  can be formed.  $\text{H}_2$  can effectively only exist at temperatures below  $\sim 10^3 \text{ K}$ , assuming a realistic desorption energy of  $3 \times 10^4 \text{ K}$  for chemisorbed H atoms (see Cazaux & Spaans 2004). The first step of SÍGAME is therefore to cool some portion of the hot SPH gas down to  $T_{\text{k}} \lesssim 10^3 \text{ K}$ , i.e., a tempera-

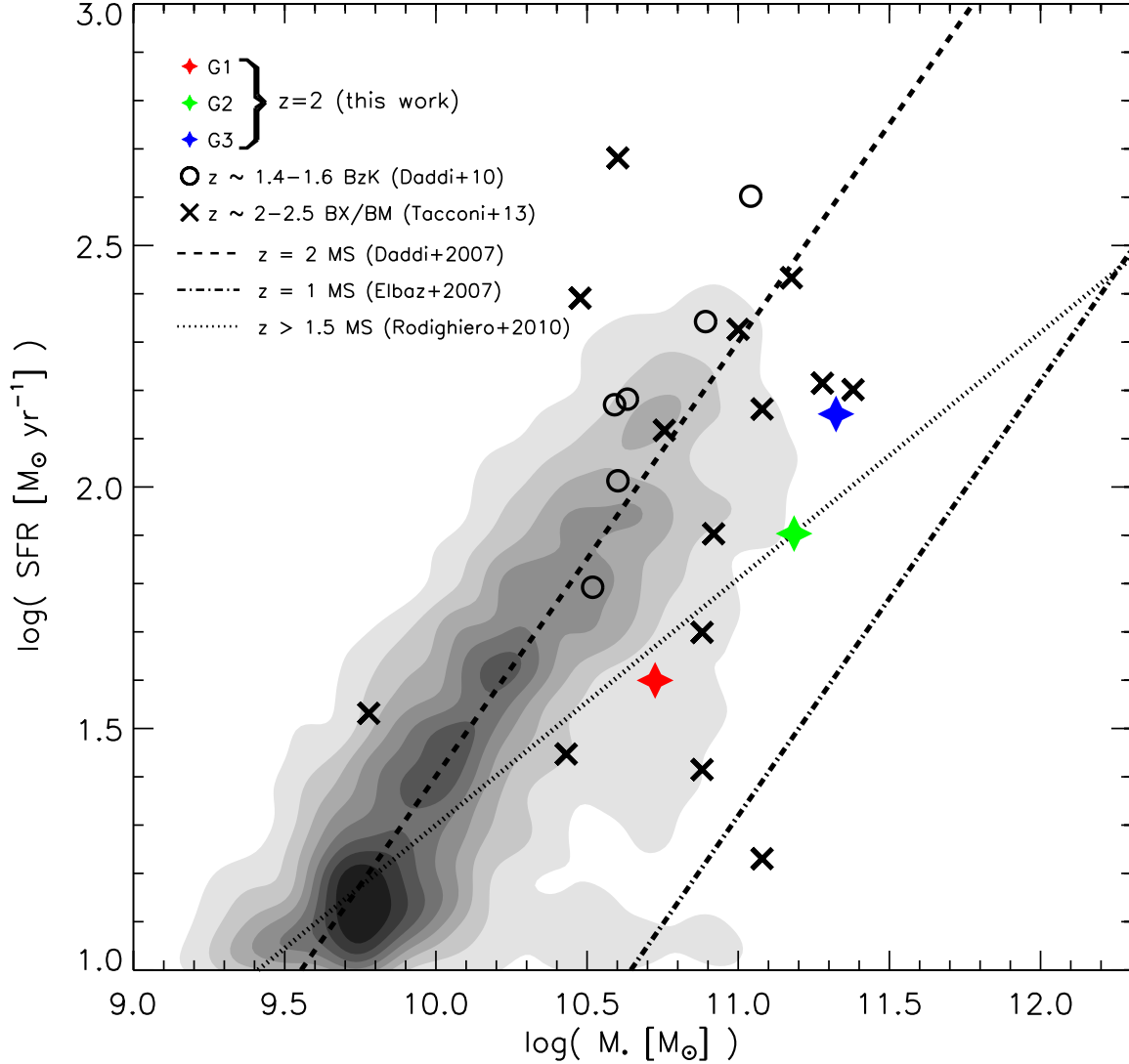


**Figure 2.** Position of the three model galaxies studied here (G1, G2 and G3 with red, green and blue stars respectively), on a SFR- $M_*$  diagram. The grey filled contours show the  $z \sim 2$  number density of 3754  $1.4 < z < 2.5$  galaxies from the NEWFIRM Medium-Band Survey (Whitaker et al. 2011). The dashed, dash-dotted and dotted lines indicate the SFR- $M_*$  relation at  $z = 2$  (Daddi et al. 2007),  $z = 1$  (Elbaz et al. 2007) and  $z > 1.5$  (Rodighiero et al. 2010), respectively. Also shown are six  $z \sim 1.4 - 1.6$  BzK galaxies (black circles; Daddi et al. 2010) and 14  $z \sim 2 - 2.5$  Bx/BM galaxies (black crosses; Tacconi et al. 2013). The BzK galaxies are from top to bottom: BzK-12591, BzK-21000, BzK-16000, BzK-17999, BzK-4171 and BzK-2553 (following the naming convention of Daddi et al. 2010).

ture range characteristic of a warm and cold neutral medium for which we can meaningfully employ a prescription for the formation of  $H_2$ .

SÍGAME employs the standard cooling and heating mechanisms pertaining to a hot, partially ionised gas. Cooling occurs primarily via emission lines from H, He, C, O, N, Ne, Mg, Si, S, Ca, and Fe in their atomic and ionised states, with the relative importance of these radiative cooling lines depending on the temperature (Wiersma et al. 2009). In addition to these emission lines, electron recombination with ions

can cool the gas, as recombining electrons take away kinetic energy from the plasma, a process which is important at temperatures  $> 10^3$  K (Wolfire et al. 2003). At similar high temperatures another important cooling mechanism is the scattering of free electrons off other free ions, whereby free-free emission removes energy from the gas (Draine 2011). Working against the cooling is heating caused by cosmic rays via the expulsion of bound electrons from atoms or the direct kinetic transfer to free electrons via Coulomb interactions (Simnett & McDonald 1969). Since this cooling

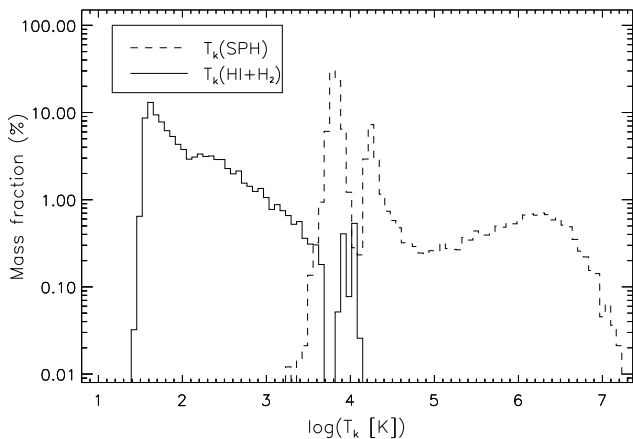


**Figure 3.** The distributions of gas kinetic temperature before (dashed histogram) and after (solid histogram) applying the heating and cooling mechanisms of eq. 1 to galaxy G1. The original hot SPH gas is seen to span a temperature range from about  $10^3$  K up to  $\sim 10^7$  K, while once the gas has been cooled the temperature distribution only barely exceeds  $\sim 10^4$  K.

step is targeted towards the hot, ionised gas, we shall ignore photo-ionization as a heating process, but include it in the subsequent temperature calculations (see Section 3.4.3).

We arrive at a first estimate of the temperature of the neutral medium by requiring energy rate equilibrium between the above mentioned heating and cooling mechanisms:

$$\Gamma_{\text{CR,H I}} = \Lambda_{\text{atoms+ions}} + \Lambda_{\text{rec}} + \Lambda_{\text{f-f}}, \quad (1)$$

where  $\Lambda_{\text{atoms+ions}}$  is the cooling rate due to atomic and ionic emission lines,  $\Lambda_{\text{rec}}$  and  $\Lambda_{\text{f-f}}$  are the cooling rates from recombination processes and free-free emission as described above, and  $\Gamma_{\text{CR,H I}}$  is the cosmic ray heating rate in atomic, partly ionised, gas. The detailed analytical expressions employed by **SÍGAME** for these heating and cooling rates are given in appendix A.

The abundances of the atoms and ions, listed above, entering the  $\Lambda_{\text{atoms+ions}}$  cooling term either have to be calculated in a self-consistent manner as part of the SPH simulation or set by hand. For our set of galaxies, the SPH simulations follow the abundances of H, C, N, O, Mg, Si, S, Ca and Fe, while for the abundances of He and Ne, we adopt solar mass fractions of 0.2806 and  $10^{-4}$ , respectively, as used in Wiersma et al. (2009).

$\Gamma_{\text{CR,H I}}$  depends on the *primary* cosmic ray ionization rate ( $\zeta_{\text{CR}}$ ), a quantity that is set by the number density of supernovae since they are thought to be the main source of CRs (Ackermann et al. 2013). In **SÍGAME**, this is accounted for by parameterizing  $\zeta_{\text{CR}}$  as a function of the *local* star formation rate density (SFRD) as it varies across the simulated galaxy. The details of this parameterization are deferred to Section 3.4.3.

It is important to emphasize that a) the ionization fraction of the gas depends on the *total* cosmic ray ionization rate (i.e.,  $\zeta_{\text{CR}}$  corrected for secondary ionizations of H and He), the gas temperature ( $T_k$ ), and H I density ( $n_{\text{H I}}$ ); and b) these quantities are interdependent (see Pelupessy (2005)). In other words, for a fixed  $\zeta_{\text{CR}}$ , all terms in eq. 1 depend on

$T_k$ ,  $n_{\text{H I}}$ , and the electron density ( $n_e$ ), see appendix A. The latter is calculated taking into account the ionization of H and He (with a procedure kindly provided by I. Pelupessy; see also Pelupessy (2005)), and is a function of both  $T_k$  and  $\zeta_{\text{CR}}$ . Since,  $n_{\text{H I}}$  is set by the molecular gas mass fraction ( $f'_{\text{mol}}$ ), which in turn also depends on  $T_k$  (see Section 3.3 on how  $f'_{\text{mol}}$  is calculated), eq. 1 has to be solved in an iterative fashion until consistent values for  $T_k$ ,  $n_e$ , and  $f'_{\text{mol}}$  are reached. Example solutions are given in Figure A1 in Appendix A.

The temperature distribution that results from solving eq. 1 for every SPH particle in the G1 simulation is shown in Figure 3 (very similar distributions are obtained for G2 and G3). The gas has been cooled to  $T_k \lesssim 10^4$  K, with temperatures extending down to 25, 30 and 27 K respectively for G1, G2 and G3. We identify this gas as the warm neutral medium (WNM) and the cold neutral medium (CNM), and it is from this gas phase that we shall construct our molecular gas phase in the subsequent sections.

### 3.3 H I to H<sub>2</sub> conversion

For the determination of the molecular gas mass fraction associated with each SPH gas particle we use the prescription of Pelupessy et al. (2006), inferred by equating the formation rate of H<sub>2</sub> on dust grains with the photodissociation rate of H<sub>2</sub> by Lyman-Werner band photons, and taking into account the self-shielding capacity of H<sub>2</sub> and dust extinction. We ignore H<sub>2</sub> production in the gas phase (cf., Christensen et al. 2012) since only in diffuse low metallicity ( $\lesssim 0.1 Z_{\odot}$ ) gas is this thought to be the dominant formation route (Norman & Spaans 1997), and so should not be relevant in our model galaxies that have mean metallicities  $Z' > 1$  (see Table 1) and very little gas exists at  $Z' < 0.1$  (see Figure C1 in Appendix C). We adopt a steady-state for the H I  $\rightarrow$  H<sub>2</sub> transition, meaning that we ignore any time dependence owing to temporal changes in the UV field strength and/or disruptions of GMCs, both of which can occur on similar time scales as the H<sub>2</sub> formation. This has been shown to be a reasonable assumption for environments with metallicities  $\gtrsim 0.01 Z_{\odot}$  (Narayanan et al. 2011; Krumholz & Gnedin 2011).

The first step is to derive the FUV field strength,  $G'_0$ , which sets the H I  $\rightarrow$  H<sub>2</sub> equilibrium. In **SÍGAME**,  $G'_0$  consists of a spatially varying component that scales with the local SFRD ( $\text{SFRD}_{\text{local}}$ ) in different parts of the galaxy on top of a constant component set by the total stellar mass of the galaxy. This is motivated by Seon et al. (2011) who measured the average FUV field strength in the MW ( $G'_{0,\text{MW}}$ ) and found that about half comes from star light directly with the remainder coming from diffuse background light. We shall assume that in the MW the direct stellar contribution to  $G'_{0,\text{MW}}$  is determined by the average SFRD ( $\text{SFRD}_{\text{MW}}$ ), while the diffuse component is fixed by the stellar mass ( $M_{*,\text{MW}}$ ). From this assumption, i.e., by calibrating to MW values, we derive the desired scaling relation for  $G'_0$  in our simulations:

$$G'_0 = G'_{0,\text{MW}} \left( 0.5 \frac{\text{SFRD}_{\text{local}}}{\text{SFRD}_{\text{MW}}} + 0.5 \frac{M_*}{M_{*,\text{MW}}} \right), \quad (2)$$

where  $G'_{0,\text{MW}} = 0.6 \text{ Habing}$  (Seon et al. 2011), and  $M_{*,\text{MW}} = 6 \times 10^{10} M_{\odot}$  (McMillan 2011). For  $\text{SFRD}_{\text{MW}}$



we adopt  $0.0024 \text{ M}_\odot \text{ yr}^{-1} \text{ kpc}^{-3}$ , inferred from the average SFR within the central 10 kpc of the MW ( $0.3 \text{ M}_\odot \text{ yr}^{-1}$ ; Heiderman et al. 2010) and within a column of height equal to the scale height of the young stellar disk (0.2 kpc; Bovy et al. 2012) of the MW disk.  $\text{SFRD}_{\text{local}}$  is the SFRD ascribed to a given SPH particle, and is calculated as the volume-averaged SFR of all SPH particles within a 5 kpc radius. Note, that the stellar mass sets a lower limit on  $G'_0$ , which for G1, G2, and G3 are 0.22, 0.62, and 0.88 Habing, respectively.

Next, the gas upon which the FUV field impinges is assumed to reside in logotropic clouds, i.e., clouds with radial density profiles given by  $n(r) = n_{\text{H,ext}} (r/R)^{-1}$ , where  $n_{\text{H,ext}}$  is the density at the cloud radius  $R$ . From Pelupessy et al. (2006) we then have that the molecular gas mass fraction, including heavier elements than hydrogen, of each cloud is given by<sup>1</sup>:

$$f'_{\text{mol}} \equiv \frac{m_{\text{mol}}}{m_{\text{SPH}}} = \exp \left[ -4 \frac{A_{\text{v}}^{(\text{tr})}}{\langle A_{\text{v}} \rangle} \right]. \quad (3)$$

Here  $\langle A_{\text{v}} \rangle$  is the area-averaged visual extinction of the cloud and  $A_{\text{v}}^{(\text{tr})}$  is the extinction through the outer layer of neutral hydrogen. The mean extinction  $\langle A_{\text{v}} \rangle$  is calculated from metallicity and average cloud density,  $\langle n_{\text{H}} \rangle$ :

$$\langle A_{\text{v}} \rangle = 7.21 \times 10^{-22} Z' \langle n_{\text{H}} \rangle R, \quad (4)$$

where  $\langle n_{\text{H}} \rangle R$  is set by a density-size relation normalized by the external boundary pressure,  $P_{\text{ext}}$ , of virialized cloud:

$$\langle n_{\text{H}} \rangle R / \text{pc} = n_{\text{ds}} \left( \frac{P_{\text{ext}} / k_{\text{B}}}{10^4 \text{ cm}^{-3} \text{ K}} \right)^{1/2}, \quad (5)$$

where the normalization constant is set to  $n_{\text{ds}} = 10^3 \text{ cm}^{-3}$ , motivated by studies of molecular clouds in the MW (Larson 1981; Wolfire et al. 2003; Heyer & Brunt 2004) (note that Pelupessy et al. (2006) uses  $1520 \text{ cm}^{-2}$ ). The external hydrostatic pressure for a rotating disk of gas and stars is calculated at mid-plane following Swinbank et al. (2011):

$$P_{\text{tot}} \approx \frac{\pi}{2} G \Sigma_{\text{gas}} \left[ \Sigma_{\text{gas}} + \left( \frac{\sigma_{\text{gas}\perp}}{\sigma_{*\perp}} \right) \Sigma_* \right], \quad (6)$$

where  $\sigma_{\text{gas}\perp}$  and  $\sigma_{*\perp}$  are the local vertical velocity dispersions of gas and stars respectively, and  $\Sigma$  denotes surface densities of the same. These quantities are all calculated directly from the simulation output, using the neighbouring SPH particles within 1 kpc. neighbouring particles within two smoothing lengths, weighted by mass, density and the cubic spline kernel (see also Monaghan 2005). For a logotropic density profile, the external density is given by  $n_{\text{H,ext}} = 2/3 \langle n_{\text{H}} \rangle$ , where we approximate  $\langle n_{\text{H}} \rangle$  with the original SPH gas density. The external cloud pressure that enters in eq. 5, is assumed to be equal to  $P_{\text{tot}} / (1 + \alpha_0 + \beta_0)$  for relative cosmic and magnetic pressure contributions of  $\alpha_0 = 0.4$  and  $\beta_0 = 0.25$  (Elmegreen 1989; Swinbank et al. 2011). For the MW,  $P_{\text{ext}} / k_{\text{B}} \sim 10^4 \text{ cm}^{-3} \text{ K}$  (Elmegreen 1989), but as shown in Fig. C1 in Appendix C, our model galaxies span a

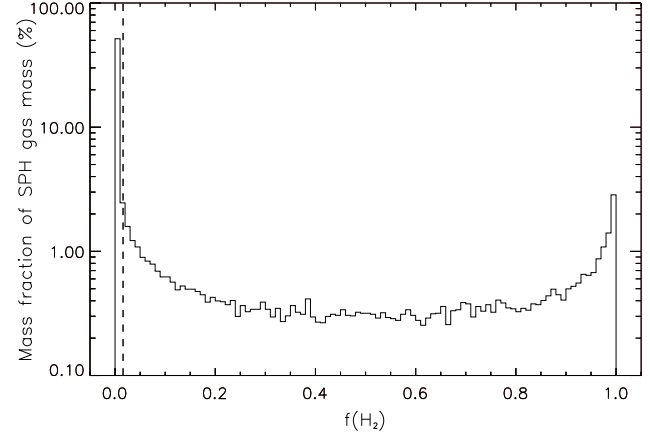


**Figure 4.** The distribution of the  $\text{H}_2$  gas mass fraction of the SPH particles in G1 calculated according to eq. 3 (solid line histogram). Similar distributions are found for G2 and G3. The lower limit on  $f'_{\text{mol}}$ , defined as described in Section 3.4.1, is indicated by the dashed vertical line.

wide range in  $P_{\text{ext}} / k_{\text{B}}$  of  $\sim 10^2 - 10^7 \text{ cm}^{-3} \text{ K}$ . In order to best account for their  $z \sim 2$  nature, we will scale the density-size relation in eq. 5 and the  $\sigma_{\text{v}}$ -size relation with  $P_{\text{ext}}$  (see Section 3.5).

For  $A_{\text{v}}^{(\text{tr})}$ , the following expression is provided by Pelupessy et al. (2006):

$$A_{\text{v}}^{(\text{tr})} = 1.086 \nu \xi_{\text{FUV}}^{-1} \times \ln \left[ 1 + \frac{G'_0}{\nu \mu S_{\text{H}}(T_{\text{k}})} \sqrt{\frac{\xi_{\text{FUV}}}{Z' T_{\text{k}}}} \right], \quad (7)$$

where  $\xi_{\text{FUV}}$  is the ratio between dust FUV absorption cross section ( $\sigma$ ) and the effective grain surface area ( $\sigma_{\text{d}}$ ), and is set to  $\xi_{\text{FUV}} = \sigma / \sigma_{\text{d}} = 3$ .  $S_{\text{H}} = (1 + 0.01 T_{\text{k}})^{-2}$  is the probability that H I atoms stick to grain surfaces, where  $T_{\text{k}}$  is the kinetic gas temperature (determined in an iterative way as explained in Section 3.2). Furthermore,  $\nu = n_{\text{H,ext}} R \sigma (1 + n_{\text{H,ext}} R \sigma)^{-1}$ , and  $\mu$  (set to 3.5 as suggested by Pelupessy et al. 2006) is a parameter which incorporates the uncertainties associated with primarily  $S_{\text{H}}$  and  $\sigma_{\text{d}}$ .

Following the above prescription SÍGAME determines the molecular gas mass fraction and thus the molecular gas mass ( $m_{\text{mol}} = f'_{\text{mol}} m_{\text{SPH}}$ ) associated with each SPH particle. Depending on the environment (e.g.,  $G'_0$ ,  $Z'$ ,  $T_{\text{k}}$ ,  $P_{\text{ext}}$ , ...), the fraction of the SPH gas converted into  $\text{H}_2$  can take on any value between 0 and 1, as seen from the  $f'_{\text{mol}}$  distribution of G1 in Figure 4. Overall, the total mass fraction of the SPH gas in G1, G2, and G3 (i.e., within  $R_{\text{cut}}$ ) that is converted to molecular gas is 29%, 52% and 34%, respectively.

### 3.4 Structure of the molecular gas

Molecular gas is known to clump on scales  $\lesssim 100 \text{ pc}$ , significantly below the typical resolution in simulations of galaxy evolution, thus posing a general problem when modelling molecular emission lines (Narayanan et al. 2011; Popping et al. 2014; Narayanan & Krumholz 2014). In relatively undisturbed, moderately star-forming galaxies, molecular

<sup>1</sup> We will use lower case  $m$  when dealing with individual SPH particles. Furthermore,  $f'_{\text{mol}}$  is not to be confused with  $f_{\text{mol}}$  describing the total molecular gas mass fraction of a galaxy and to be introduced in Section 4.

gas is believed to be distributed in giant molecular clouds (GMCs) of sizes  $\sim 6-60$  pc with internal substructures similar to those observed in the MW (Kauffmann et al. 2010), and as suggested by simulations (e.g. Vázquez-Semadeni et al. 2010). Having determined the molecular gas mass fractions, **SÍGAME** proceeds by distributing the molecular gas into GMCs, and calculates the masses and sizes, along with the internal density and temperature structure, for each GMC as described in the following.

### 3.4.1 GMC masses and sizes

The molecular gas associated with a given SPH particle is divided into a number of GMCs, the masses of which are assumed to follow a power-law spectrum of the form:

$$\frac{dN}{dm_{\text{GMC}}} \propto m_{\text{GMC}}^{-\beta}. \quad (8)$$

For the MW disk and Local Group galaxies  $\beta \simeq 1.8$  (Blitz et al. 2007), and this will be our default choice unless otherwise stated. Lower and upper mass cut-offs at  $10^4 M_\odot$  and  $10^6 M_\odot$ , respectively, are enforced in order to span the mass range observed by Blitz et al. (2007). A similar approach was adopted by Narayanan et al. (2008b,c). Note, in the case of G1 the upper cut-off on the GMC masses is in fact set by the mass resolution of the SPH simulation ( $6.3 \times 10^5 h^{-1} M_\odot$ ). For G1, typically  $\lesssim 30$  GMCs are created in this way per SPH particle, while for G2 and G3, which were run with SPH gas particles masses almost an order of magnitude higher, as much as  $\sim 100$  GMCs can be extracted from a given SPH particle for  $\beta = 1.8$ . Figure 5 shows the resulting mass distribution of all the GMCs in G1, along with the distribution of molecular mass associated with the SPH gas particles prior to it being divided into GMCs. The net effect of re-distributing the  $H_2$  mass into GMCs is a mass distribution dominated by relatively low cloud masses, which is in contrast to the relatively flat SPH  $H_2$  mass distribution. Note, the lower cut-off at  $m_{\text{GMC}} = 10^4 M_\odot$  implies that if the molecular gas mass associated with an SPH particle (i.e.,  $m_{\text{mol}} = f'_{\text{mol}} m_{\text{SPH}}$ ) is less than this lower limit it will not be re-distributed into GMCs. Since  $m_{\text{SPH}}$  is constant in our simulations ( $6.3 \times 10^5 h^{-1} M_\odot$  for G1 and  $4.7 \times 10^6 h^{-1} M_\odot$  for G2 and G3) the lower limit imposed on  $m_{\text{GMC}}$  translates directly into a lower limit on  $f'_{\text{mol}}$  (0.016 for G1 and 0.002 for G2 and G3, shown as a dashed vertical line for G1 in Figure 4). As a consequence, 0.2, 0.005 and 0.01 % of the molecular gas in G1, G2, and G3, respectively, does not end up in GMCs. These are negligible fractions and the molecular gas they represent can therefore be safely ignored.

The sizes,  $R_{\text{GMC}}$ , of the GMCs are derived via application of the virial theorem, by which  $R_{\text{GMC}}$  depends on the GMC mass and the external pressure,  $P_{\text{ext}}$ :

$$\frac{R_{\text{GMC}}}{\text{pc}} = \left( \frac{P_{\text{ext}}/k_B}{10^4 \text{ cm}^{-3} \text{ K}} \right)^{-1/4} \left( \frac{m_{\text{GMC}}}{290 M_\odot} \right)^{1/2}, \quad (9)$$

and  $\sigma_v$  depends on  $R_{\text{GMC}}$  and  $P_{\text{ext}}$  via:

$$\frac{\sigma_v}{\text{km s}^{-1}} = 1.2 \left( \frac{P_{\text{ext}}/k_B}{10^4 \text{ cm}^{-3} \text{ K}} \right)^{1/4} \left( \frac{R_{\text{GMC}}}{\text{pc}} \right)^{1/2}, \quad (10)$$

see, e.g., Elmegreen (1989); Swinbank et al. (2011). Figure 6 shows the resulting distribution of GMC sizes ( $R_{\text{GMC}}$ ) for G1, for the two GMC mass spectra investigated here (see

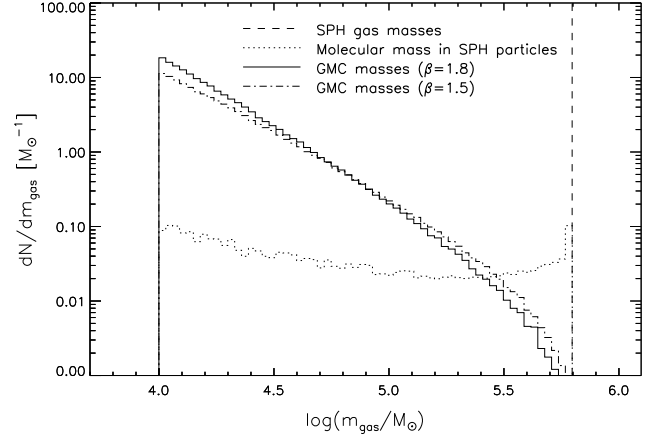


**Figure 5.** The distribution of GMC masses in G1 obtained by applying eq. 8, with  $\beta = 1.8$  (solid histogram) and  $\beta = 1.5$  (dash-dotted histogram), to the total molecular gas masses associated with SPH particles (distribution shown as dotted histogram). The dashed vertical line indicates the SPH gas mass resolution of the simulation ( $= 6.3 \times 10^5 h^{-1} M_\odot$  in the case of G1).

beginning of this Section). Upper and lower limits on cloud sizes of  $\sim 0.07$  pc and  $\sim 60$  pc, respectively, are set by the maximum and minimum GMC masses and pressure in G1.

Since observations have indicated that the shape of the GMC mass spectrum might be different at high redshift, in particular in gas-rich systems harbouring a high-pressure ISM and massive star-forming clumps of molecular gas (e.g. Swinbank et al. 2011; Leroy et al. 2015), we examined the effects of adopting a different index, namely  $\beta = 1.5$ , corresponding to virialized ( $\sigma_v \propto \sqrt{R}$ ) clouds (Padoan & Nordlund 2002). The mass distribution resulting from this lower value of  $\beta$  is more top-heavy than our adopted spectrum (see Figure 5), and as a result there are more clouds with sizes  $R_{\text{GMC}} \gtrsim 10$  pc and fewer clouds at smaller radii (Figure 6). Yet, the total amount of molecular gas in our galaxies does not change significantly between  $\beta = 1.8$  and  $\beta = 1.5$ , and we therefore conclude that our simulation results are robust against (reasonable) changes in the mass-spectrum.

As the final step, the GMCs are placed randomly around the position of their ‘parent’ SPH particle, albeit with an inverse proportionality between radial displacement and mass of the GMC. The latter is done in order to retain the mass distribution of the original galaxy simulation as best as possible. The GMCs are assigned the same bulk velocity,  $\bar{v}$ ,  $Z'$ ,  $G'_0$  and  $\zeta_{\text{CR}}$  as their ‘parent’ SPH particle.

### 3.4.2 GMC density structure

In order to ensure a finite central density in our GMCs, **SÍGAME** adopts a Plummer radial density profile (e.g., Gieles et al. 2006; Miettinen et al. 2009):

$$n_{H_2}(R)[\text{cm}^{-3}] = 20.23 \frac{3m_{\text{GMC}}[M_\odot]}{4\pi 1.36(R_p[\text{pc}])^3} \left( 1 + \frac{R^2}{R_p^2} \right)^{-5/2}, \quad (11)$$

where  $R_p$  is the so-called Plummer radius, which we set to  $R_p = 0.1 R_{\text{GMC}}$ . The latter allows for a broad range in gas



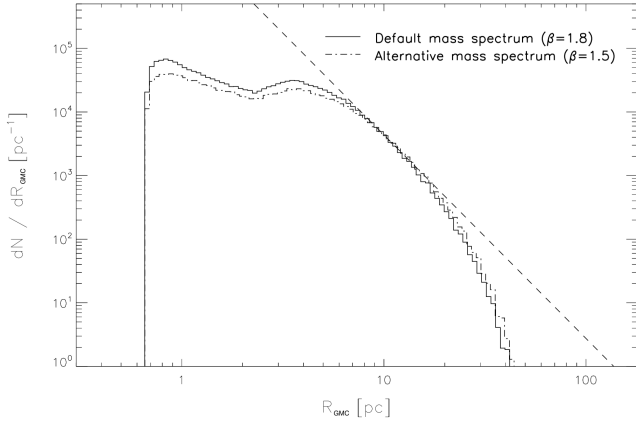


**Figure 6.** The distribution of GMC radii in G1 for the adopted cloud mass spectrum with  $\beta = 1.8$  (solid histogram) and for a slightly modified spectrum with  $\beta = 1.5$  (dash-dotted histogram). Similar distributions are found for G2 and G3. The dashed line shows the best-fit power-law to the distribution:  $\frac{dN}{dR_{\text{GMC}}} \propto R_{\text{GMC}}^{-3.2}$ . Observations of clouds in the outer Galactic disk found a size distribution with a power-law slope of  $-3.2 \pm 0.1$  over a similar size range (Heyer et al. 2001).

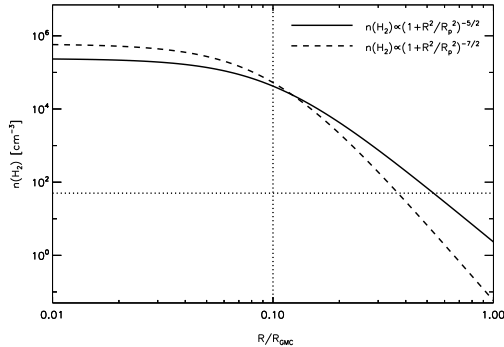


**Figure 7.** Plummer density profiles (eq. 11) with power-law exponents of  $-5/2$  (solid line) and  $-7/2$  (dashed line) for a GMC mass of  $10^4 M_{\odot}$  and an external pressure of  $P_{\text{ext}}/k_B = 10^4 \text{ K cm}^{-3}$ . The corresponding cloud radius is  $R_{\text{GMC}} = 5.9 \text{ pc}$  (eq. 9). The vertical dotted line marks the Plummer radius ( $= 0.1 R_{\text{GMC}}$ ), and the horizontal dotted line the  $n_{\text{H}_2}$  value ( $50 \text{ cm}^{-3}$ ) below which CO is assumed to photo-dissociate in our simulations.

densities throughout the clouds, from  $\sim 10^6 \text{ cm}^{-3}$  in the central parts to a few  $10 \text{ cm}^{-3}$  further out. The factor 1.36 in the denominator accounts for the presence of helium in the GMC. We test the effects of a steeper GMC density profile on our final results by adopting an exponent of  $-7/2$  in eq. 11 and re-running our simulations. Plummer profiles with exponents  $-5/2$  and  $-7/2$  are shown in Figure 7 for a GMC with mass of  $10^4 M_{\odot}$  and external pressure  $10^4 \text{ K cm}^{-3}$ .

### 3.4.3 GMC thermal structure

Having established the masses, sizes, and density structure of the GMCs, SÍGAME next solves for the kinetic temperature throughout the clouds. This means balancing the rele-

vant heating and cooling mechanisms as a function of cloud radius.

GMCs are predominantly heated by FUV photons (via the photo-electric effect) and cosmic rays. For the strength of the FUV field impinging on the GMCs, we take the previously calculated values at the SPH gas particle position (eq. 2). We shall assume that the cosmic ray ionization rate scales in a similar manner, having its origin in supernovae and therefore also being closely related to nearby star formation and the total stellar mass of the galaxy:

$$\zeta_{\text{CR}} = \zeta_{\text{CR,MW}} \left( 0.5 \frac{\text{SFRD}_{\text{local}}}{\text{SFRD}_{\text{MW}}} + 0.5 \frac{M_{*}}{M_{*,\text{MW}}} \right) \quad (12)$$

where  $\text{SFRD}_{\text{local}}$ ,  $\text{SFRD}_{\text{MW}}$  and  $M_{*,\text{MW}}$  are as described in Section 3.3, and  $\zeta_{\text{CR}}$  is scaled to the ‘canonical’ MW value of  $\zeta_{\text{CR,MW}} = 3 \times 10^{-17} \text{ s}^{-1}$  (e.g. Webber 1998). While the FUV radiation is attenuated by dust and therefore does not heat the GMC centres significantly, cosmic rays can penetrate these dense regions and heat the gas there (Papadopoulos et al. 2011). For this reason we will attenuate the FUV field, but not the cosmic ray field, assuming that the latter keeps the same intensity throughout the GMCs. The extinction of the FUV field at a certain point within a GMC is derived by integrating the Plummer density profile from that point and out to the cloud surface, which is taken to be  $R_{\text{GMC}}$ . This H column density is converted into a visual extinction ( $A_V = N_{\text{H}}/2.2 \times 10^{21} \text{ cm}^{-2}$ ) so that attenuated FUV field becomes:

$$G'_{0,\text{att}} = G'_0 e^{-1.8 A_V}, \quad (13)$$

where the factor of 1.8 is the adopted conversion from visual to FUV extinction (Black & Dalgarno 1977). We calculate the temperature throughout each GMC via the following heating and cooling rate balance:

$$\Gamma_{\text{PE}} + \Gamma_{\text{CR,H}_2} = \Lambda_{\text{H}_2} + \Lambda_{\text{CO}} + \Lambda_{\text{OI}} + \Lambda_{\text{CI}} + \Lambda_{\text{gas-dust}}. \quad (14)$$

$\Gamma_{\text{PE}}$  is the photo-electric heating by FUV photons, and  $\Gamma_{\text{CR,H}_2}$  is the cosmic ray heating in molecular gas.  $\Lambda_{\text{H}_2}$  is the cooling rate of the two lowest  $\text{H}_2$  rotational lines (S(0) and S(1)), and  $\Lambda_{\text{CO}}$  is the cooling rate of the combined CO rotational ladder.  $\Lambda_{\text{gas-dust}}$  is the cooling rate due to interactions between gas molecules and dust particles, which only becomes important at densities above  $10^4 \text{ cm}^{-3}$  (e.g., Goldsmith 2001; Glover & Clark 2012).  $\Lambda_{\text{CI}}$  and  $\Lambda_{\text{OI}}$  are the cooling rates due to [CII] and [OI] line emission, respectively, the strongest cooling lines in neutral ISM. The abundances of carbon and oxygen used in the prescriptions for their cooling rates, scale with the cloud metallicity, while the CO cooling scales with the relative CO to neutral carbon abundance ratio, set by the molecular density (see Appendix B).

The dust temperature,  $T_{\text{dust}}$ , used for  $\Lambda_{\text{gas-dust}}$  in eq. 14 is set by the equilibrium between absorption of FUV and the emission of IR radiation by the dust grains. We adopt the approximation given by Tielens (2005):

$$\frac{T_{\text{dust}}}{\text{K}} \simeq 33.5 \left( \frac{a}{1 \mu\text{m}} \right)^{-0.2} \left( \frac{G'_{0,\text{att}}}{10^4 \text{ Habing}} \right)^{0.2}, \quad (15)$$

where  $G'_{0,\text{att}}$  is the dust-attenuated FUV field (eq. 13) and  $a$  is the grain size, which we set to  $1 \mu\text{m}$  for simplicity. Values for  $T_{\text{dust}}$  using eq. 15 range from 0 to 8.9 K, but we enforce a lower limit on  $T_{\text{dust}}$  equal to the  $z = 2$  CMB temperature

of 8.175 K.  $T_{\text{dust}}$  is therefore essentially constant ( $\sim 8 - 9$  K) throughout the inner region of the GMC models, similar to the value of  $T_{\text{dust}} = 8$  K adopted by Papadopoulos & Thi (2013) for CR-dominated cores. Analytical expressions for all of the above heating and cooling rates are given in Appendix B, which also shows their relative strengths as a function of density for two example GMCs (Figure B1).

Figure C2 in Appendix C shows the resulting  $T_{\text{k}}$  versus  $n_{\text{H}_2}$  behaviour for 80 GMCs spanning a broad range of GMC masses, metallicities, and star formation rate densities. As seen in the displayed GMC models, some general trends can be inferred from the  $T_{\text{k}} - n_{\text{H}_2}$  diagrams. At fixed metallicity and mass, an increase in FUV radiation field,  $G'_0$  (and therefore also CR ionization rate,  $\zeta_{\text{CR}}$ ), leads to higher temperatures throughout the models. In the outer regions this is due primarily to the increased photoelectric heating, while in the inner regions, heating by the unattenuated cosmic rays takes over as the dominating heating mechanism (Figure B1). Keeping  $G'_0$  (and  $\zeta_{\text{CR}}$ ) fixed, lower  $T_{\text{k}}$ -levels and shallower  $T_{\text{k}} - n_{\text{H}_2}$  gradients are found in GMCs with higher metallicities,  $Z'$ . Both these trends are explained by the fact that the  $[\text{CII}]$  and  $[\text{OI}]$  cooling rates scale linearly with  $Z'$  (see Appendix B).

Moving from the outskirts and inward towards the GMC centres (i.e., towards higher densities),  $T_{\text{k}}$  drops as the attenuation of  $G'_0$  reduces the photoelectric heating. However, the transition from the cooling by  $[\text{CII}]$  to the less efficient cooling mechanism by CO lines, causes a local increase in  $T_{\text{k}}$  at  $n_{\text{H}_2} \sim 10^3 - 10^{4.5} \text{ cm}^{-3}$ , as also seen in the detailed GMC simulations by Glover & Clark (2012). The exact density at which this ‘bump’ in  $T_{\text{k}}$  depends strongly on the mass of the GMC, which is an effect of the chosen mass distribution within the GMCs. Our choice of the Plummer model for the radial density profile means that the extinction,  $A_{\text{V}}$ , at a certain density increases with GMC mass. This in turn decreases the FUV heating, and as a result the  $T_{\text{k}} - n_{\text{H}_2}$  curve moves to lower densities with increasing GMC mass.

As the density increases towards the cloud centres (i.e.,  $n_{\text{H}_2} \gtrsim 10^{4-5} \text{ cm}^{-3}$ ) molecular line cooling and also gas-dust interactions become increasingly efficient and start to dominate the cooling budget. The  $T_{\text{k}} - n_{\text{H}_2}$  curves are seen to be insensitive to changes in  $Z'$ , which is expected since the dominant heating and cooling mechanisms in these regions do not depend on  $Z'$ . Eventually, in the very central regions of the clouds, the gas reaches temperatures close to that of the ambient CMB radiation field, irrespective of the overall GMC properties and the conditions at the surface (Figure B1).

#### 3.4.4 GMC grid models

The  $T_{\text{k}} - n_{\text{H}_2}$  curve for a given GMC is determined by the following basic quantities:

- The FUV radiation ( $G'_0$ ), and with that the cosmic ray field strength,  $\zeta_{\text{CR}}$  (proportional to  $G'_0$ ), together governing the heating of the gas.
- The GMC mass ( $m_{\text{GMC}}$ ), which (together with  $P_{\text{ext}}$ ) determines the effective radius of a cloud (eq. 9) and thus its density profile (eq. 11).

**Table 2.** Grid parameter values

$G'_0$ [Habing]	0.5, 1, 4, 7, 10, 13, 16, 19, 23, 27
$\log(m_{\text{GMC}} [\text{M}_{\odot}])$	4.0, 4.25, 4.5, 4.75, 5.0, 5.25, 5.5, 5.75, 6.0
$\log(Z/Z_{\odot})$	-1, -0.5, 0, 0.5, 1, 1.4, 1.8
$\log(P_{\text{ext}}/k_{\text{B}} [\text{K cm}^{-3}])$	4.0, 5.5, 6.5

- The local metallicity ( $Z'$ ), which influences the fraction of  $\text{H}_2$  gas and plays an important role in cooling the gas.
- The external pressure ( $P_{\text{ext}}$ ), which determines the  $m_{\text{GMC}} - R_{\text{GMC}}$  and  $\sigma_{\text{v}} - R_{\text{GMC}}$  relations.

Of these,  $G'_0$  and  $\zeta_{\text{CR}}$  are set by the local star formation rate density ( $\text{SFRD}_{\text{local}}$ ) and the total stellar mass ( $M_{\star}$ ) according to eqs. 2 and 12,  $Z'$  is taken directly from the simulations while  $m_{\text{GMC}}$  is extracted randomly from a probability distribution as explained in Section 3.4.1. The distributions of  $m_{\text{GMC}}$ ,  $Z'$ ,  $G'_0$ ,  $\zeta_{\text{CR}}$  and  $P_{\text{ext}}/k_{\text{B}}$  for each of the galaxies G1, G2 and G3 are shown in Figure C1.

There are more than 100,000 GMCs in a single model galaxy and, as Figure C1 shows, they span a wide range in  $G'_0$ ,  $m_{\text{GMC}}$ ,  $Z'$  and  $P_{\text{ext}}/k_{\text{B}}$ . Thus, in order to shorten the computing time, we calculated  $n_{\text{H}_2}$  and  $T_{\text{k}}$  profiles for a set of 630 GMCs, chosen to appropriately sample the distributions in  $G'_0$ ,  $m_{\text{GMC}}$  and  $Z'$  at certain grid values (listed in Table 2, and marked by vertical black lines in Figure C1). Our default for  $P_{\text{ext}}/k_{\text{B}}$  will be a MW-like value of  $10^4 \text{ K cm}^{-3}$ , but we also constructed the above grid for  $P_{\text{ext}}/k_{\text{B}} = 10^{5.5} \text{ K cm}^{-3}$  and  $10^{6.5} \text{ K cm}^{-3}$ . In addition we test the two radial GMC density profiles defined in Section 3.4.2.  $T_{\text{k}} - n_{\text{H}_2}$  curves were calculated for each possible combination of the parameter grid values listed in Table 2 giving us a total of  $3 \times 2 \times 630 = 3780$  GMC grid models. Every GMC in our simulations was subsequently assigned the  $T_{\text{k}} - n_{\text{H}_2}$  curve of the GMC grid model closest to it in our ( $G'_0$ ,  $m_{\text{GMC}}$ ,  $Z'$ ) parameter space.

### 3.5 Radiative transfer of CO lines

**SÍGAME** assumes the density of CO follows that of the  $\text{H}_2$  gas with a fixed CO abundance equal to the Galactic value of  $[\text{CO}/\text{H}_2] = 2 \times 10^{-4}$  (Lee et al. 1996; Sofia et al. 2004, and see Section 6 for a justification of this value) everywhere in the GMCs except for  $n_{\text{H}_2} < 50 \text{ cm}^{-3}$ , where CO is not expected to survive photo-dissociation processes (e.g. Narayanan et al. 2008c). Now we are ready to solve the radiative transfer for each GMC individually and derive the emerging CO line emission from the entire galaxy.

#### 3.5.1 Individual GMCs

For the CO radiative transfer calculations we use a slightly modified version of the LIne Modeling Engine (**LIME** ver. 1.4; Brinch & Hogerheijde (2010)) - a 3D molecular excitation and radiative transfer code. **LIME** has been modified in order to take into account the redshift dependence of the CMB temperature, which is used as boundary condition for the radiation field during photon transport, and we have also introduced a redshift correction in the calculation of

physical sizes as a function of distance. We use collision rates for CO (assuming  $\text{H}_2$  as the main collision partner) from Yang et al. (2010). In LIME, photons are propagated along grid lines defined by Delaunay triangulation around a set of appropriately chosen sample points in the gas, each of which contain information on  $n_{\text{H}_2}$ ,  $T_k$ ,  $\sigma_v$ ,  $[\text{CO}/\text{H}_2]$  and  $\bar{v}$ . SÍGAME constructs such a set of sample points throughout each GMC: about 5000 points distributed randomly out to a radius of 40 pc, i.e., beyond the effective radius of all GMCs in G1, G2, and G3 (Figure 6) and in a density regime below the threshold density of  $50 \text{ cm}^{-3}$  adopted for CO survival (see previous paragraph). The concentration of sample points is set to increase towards the centre of each GMC where the density and temperature vary more drastically.

For each GMC, LIME generates a CO line data cube, i.e., a series of CO intensity maps as a function of velocity. The velocity-axis consists of 50 channels, each with a spectral resolution of  $1.0 \text{ km s}^{-1}$ , thus covering the velocity range  $v = [-25, +25] \text{ km s}^{-1}$ . The maps are 100 pc on a side and split into 200 pixels, corresponding to a linear resolution of  $0.5 \text{ pc/pixel}$  (or an angular resolution of  $5.9 \times 10^{-5}''/\text{pixel}$  at  $z = 2$ ). Intensities are corrected for arrival time delay and redshifting of photons.

Figure C3 shows the area- and velocity-integrated CO Spectral Line Energy Distributions (SLEDs) for the same 80 GMCs used in Section 3.4.3 to highlight the  $T_k - n_{\text{H}_2}$  profiles (Figure C2). The first thing to note is that the CO line fluxes increase with  $m_{\text{GMC}}$ , which is due to the increase in size, i.e., surface area of the emitting gas, with cloud mass (Section 3.4.1). Turning to the shape of the CO SLEDs, a stronger  $G'_0$  (and  $\zeta_{\text{CR}}$ ) increases the gas temperature and thus drives the SLEDs to peak at higher  $J$ -transitions. Only the higher,  $J_{\text{up}} > 4$ , transitions are also affected by metallicity, displaying increased flux with increased  $Z'$  for  $Z' \gtrsim 1$  and  $G'_0 \gtrsim 1$ . For GMCs with high  $G'_0$ , the high metallicity levels thus cause the CO SLED to peak at  $J_{\text{up}} > 8$ .

### 3.5.2 The effects of dust

Dust absorbs the UV light from young O and B stars and re-emits in the far-IR, leading to possible ‘IR pumping’ of molecular infrared sources. However, due to the large vibrational level spacing of CO, the molecular gas has to be at a temperature of at least 159 K, for significant IR pumping of the CO rotational lines to take place, when assuming a maximum filling factor of 1, as shown by Carroll & Goldsmith (1981). Most of the gas in our GMC models is at temperatures below 100 K, with only a small fraction of the gas, in the very outskirts, of the GMCs reach  $T_k > 159 \text{ K}$ , as seen in Figure C2 in Appendix C. This happens only if the metallicity is low ( $Z' \leq 0.1$ ) or in case of a combination between high FUV field ( $G'_0 \geq 4$ ) and moderate metallicity. On the other hand, the CO emission lines could be subject to dust extinction, which is however only important in extremely dust-enshrouded sources such as Arp 220 (Papadopoulos et al. 2010), and therefore not significant for our set of normal galaxies.

Upon these reflections, we have chosen not to include dust in the radiative transfer calculations of each GMC, although we mention that LIME is fully capable of including a dust component, provided that a table of dust opacities as

function of wavelength be supplied together with the input model.

## 3.6 Combining the GMC line profiles in a galaxy

The CO emission line profile is derived for each galaxy GMC by assigning to it the GMC model that corresponds to the nearest grid point (in log space for  $m_{\text{GMC}}$  and  $Z'$ ). The total line profiles of the galaxies are derived by adding the line profiles of individual GMCs to a common velocity axis at their respective projected velocities within each galaxy. This assumes that the molecular line emission from each GMC is radiatively decoupled from all other GMCs, which is a reasonable assumption due to the large velocity gradients through the galaxies ( $\sigma_v$  of  $\sim 200 - 500 \text{ km s}^{-1}$  in our model galaxies) and the relatively small internal turbulent line widths expected for the GMC (typically  $\sim 1 - 3 \text{ km s}^{-1}$  for Galactic GMCs; Heyer et al. 2009).

CO moment 0 maps are constructed by overlaying a grid of  $500 \times 500$  pixels on each galaxy and adding the area-integrated CO line profiles from all GMCs within each pixel to a common velocity axis and integrating this line profile in velocity. This way, we create maps with a fixed width of 20 kpc and a resolution of  $\sim 80 \text{ pc}$ . By integrating in area instead of velocity, we create total line profiles, and by further integrating these line profiles in velocity space, the CO SLED for the entire galaxy can be derived. All this will be examined in the following section and the results discussed further in Section 6.

## 4 SIMULATING MASSIVE $Z = 2$ MAIN SEQUENCE GALAXIES

In this section we examine the  $\text{H}_2$  surface density and CO emission maps resulting from applying SÍGAME to the three SPH galaxy simulations G1, G2, and G3 (Section 2), and we compare with existing CO observations of main sequence galaxies at  $z \sim 1 - 2.5$ . As mentioned in previous sections, our default grid will be that corresponding to a Plummer density profile and a pressure of  $P_{\text{ext}}/k_B = 10^4 \text{ cm}^{-3} \text{ K}$ , combined with a GMC mass spectrum of slope  $\beta = 1.8$ , unless otherwise stated.

### 4.1 Total molecular gas content and $\text{H}_2$ surface density maps

The total molecular gas masses of G1, G2 and G3 – obtained by summing up the GMC masses associated with all SPH particles within each galaxy (i.e.,  $M_{\text{mol}} = \sum m_{\text{GMC}} = \sum f'_{\text{mol}} m_{\text{SPH}}$ ) – are  $7.1 \times 10^9$ ,  $1.7 \times 10^{10}$ , and  $2.1 \times 10^{10} M_\odot$ , respectively, corresponding to about 34, 59 and 45 % of the original total SPH gas masses of the galaxies within  $R_{\text{cut}} = 20 \text{ kpc}$ .<sup>2</sup> The global molecular gas mass fractions (i.e.,  $f_{\text{mol}} = M_{\text{mol}}/(M_* + M_{\text{mol}})$ ) are 11.8, 9.8 and 9.1 % for G1, G2, and G3, respectively.

<sup>2</sup> These global molecular-to-SPH gas mass fractions are calculated as  $M_{\text{mol}}/M_{\text{SPH}} = \sum m_{\text{GMC}}/\sum m_{\text{SPH}}$ , where the sums are over all SPH particles.

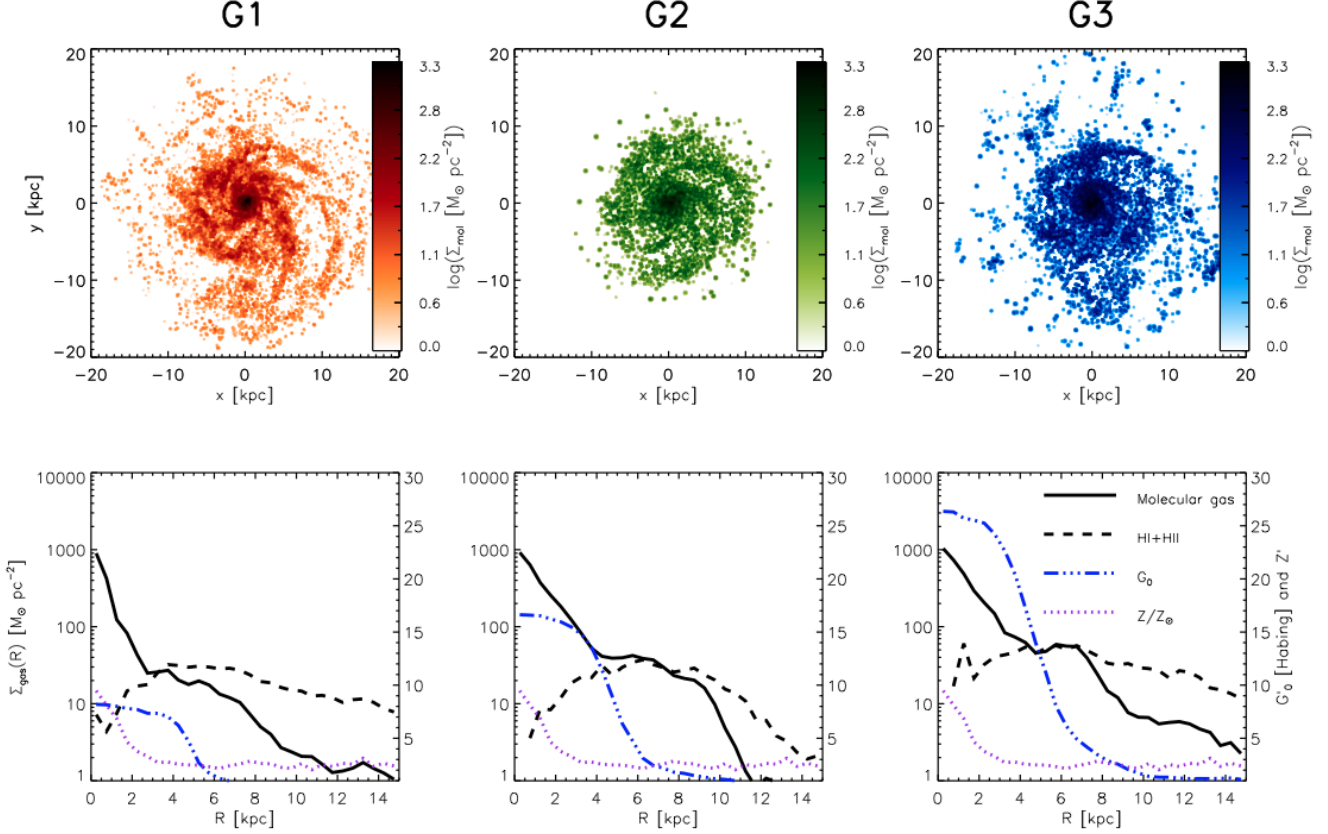


**Figure 8.** Top row: Molecular surface density maps of our model galaxies seen face-on. The maps have been smoothed using a circular Gaussian with full width at half maximum (FWHM) of 3 pixels corresponding to 0.24 kpc. Comparing to the SPH gas density maps in Figure 1 the molecular gas surface density maps are seen to trace the same spiral arms and inner disk as well as a few dense clumps further out. Bottom row: azimuthally averaged radial profiles of the  $\text{HI} + \text{HII}$  (dashed curve) and molecular (solid curve) gas surface densities, of the mean metallicity (dotted curve) and of  $G'_0$  (dot-dashed curve) – determined from 50 radial bins stretching from 0 to 15 kpc from the centre of each galaxy. The molecular gas is the result of applying the recipes in Section 3.3 to the SPH simulations presented in Section 2.2, while the  $\text{HI} + \text{HII}$  gas is the initial SPH gas mass minus the derived molecular gas mass, including a contribution from heavier elements. We estimate  $G'_0$  by averaging over the FUV fields impinging on all GMCs in each radial bin.

For the high-redshift samples we use for comparison in Figure 10,  $f_{\text{mol}}$  assumes mean values of;  $59 \pm 23\%$  for the  $z \sim 1 - 1.3$  SFGs of Magnelli et al. (2012),  $57 \pm 6\%$  for the  $z \sim 1.5$  BzKs of Daddi et al. (2010),  $48 \pm 14\%$  for the  $z \sim 1 - 2.2$  SFGs of Tacconi et al. (2013) and  $52 \pm 20\%$  for the  $z \sim 2 - 2.5$  BX/BM galaxies of Tacconi et al. (2013). The mean for all these galaxies is  $\sim 47\%$  or  $\sim 4 - 5$  times above that of our galaxies. In comparison, local star-forming galaxies are relatively gas-poor as shown by Saintonge et al. (2011), who estimated molecular masses for a sample of nearby star-forming galaxies by applying a MW-like  $\alpha_{\text{CO}}$  factor to 119 detections in  $\text{CO}(1 - 0)$  and to a stack of 103 non-detections. Correcting their molecular masses for the contribution from helium (1.36), the mean  $f_{\text{mol}}$  is only  $\sim 6.7 \pm 4.5\%$ . While our model galaxies have molecular gas mass fractions about a factor 4 – 5 below  $z \sim 1 - 2.5$  star-forming galaxies, they are within the observed range for the local counterparts. The main cause for this discrepancy between our model galaxies and observations made at  $z \sim 2$ , is most likely the relatively low SPH gas mass fractions to begin with, i.e.  $f_{\text{SPH}} = M_{\text{SPH}} / (M_{\star} + M_{\text{SPH}}) = 9 - 26\%$ , restricting  $f_{\text{mol}}$  to be below these values.

The molecular surface density ( $\Sigma_{\text{mol}}$ ) maps of G1, G2, and G3, depicting the average  $\Sigma_{\text{mol}}$  within pixels  $80 \text{ pc} \times 80 \text{ pc}$  in size, are shown in Figure 8 (top panels). The pixel size was chosen in order to avoid resolving the GMCs, which have typical sizes of  $R_{\text{GMC}} \approx 0.7 - 30 \text{ pc}$  (see Section 3.4.1).

Some molecular gas is seen to extend out to radii of  $\sim 10 \text{ kpc}$  and beyond, but generally the molecular gas concentrates within the inner regions of each galaxy. Thus, the distribution of molecular gas broadly follows the central disk and spiral arms where the SPH surface density ( $\Sigma_{\text{SPH}}$ ) is also the highest (Figure 1). The correspondence is far from one-to-one, however, as seen by the much larger extent of the SPH gas, i.e., regions where  $\text{H}_2$  has not formed despite the presence of atomic and ionized gas. This point is further corroborated in the bottom panels of Figure 8, which show azimuthally-averaged radial surface density profiles of the molecular gas and of the  $\text{HI} + \text{HII}$  gas, both including a contribution from heavier elements. In order to compare values of  $\Sigma_{\text{HI} + \text{HII}}$  and  $\Sigma_{\text{mol}}$  with observations, we set the radial bin width to 0.5 kpc – the typical radial bin size used

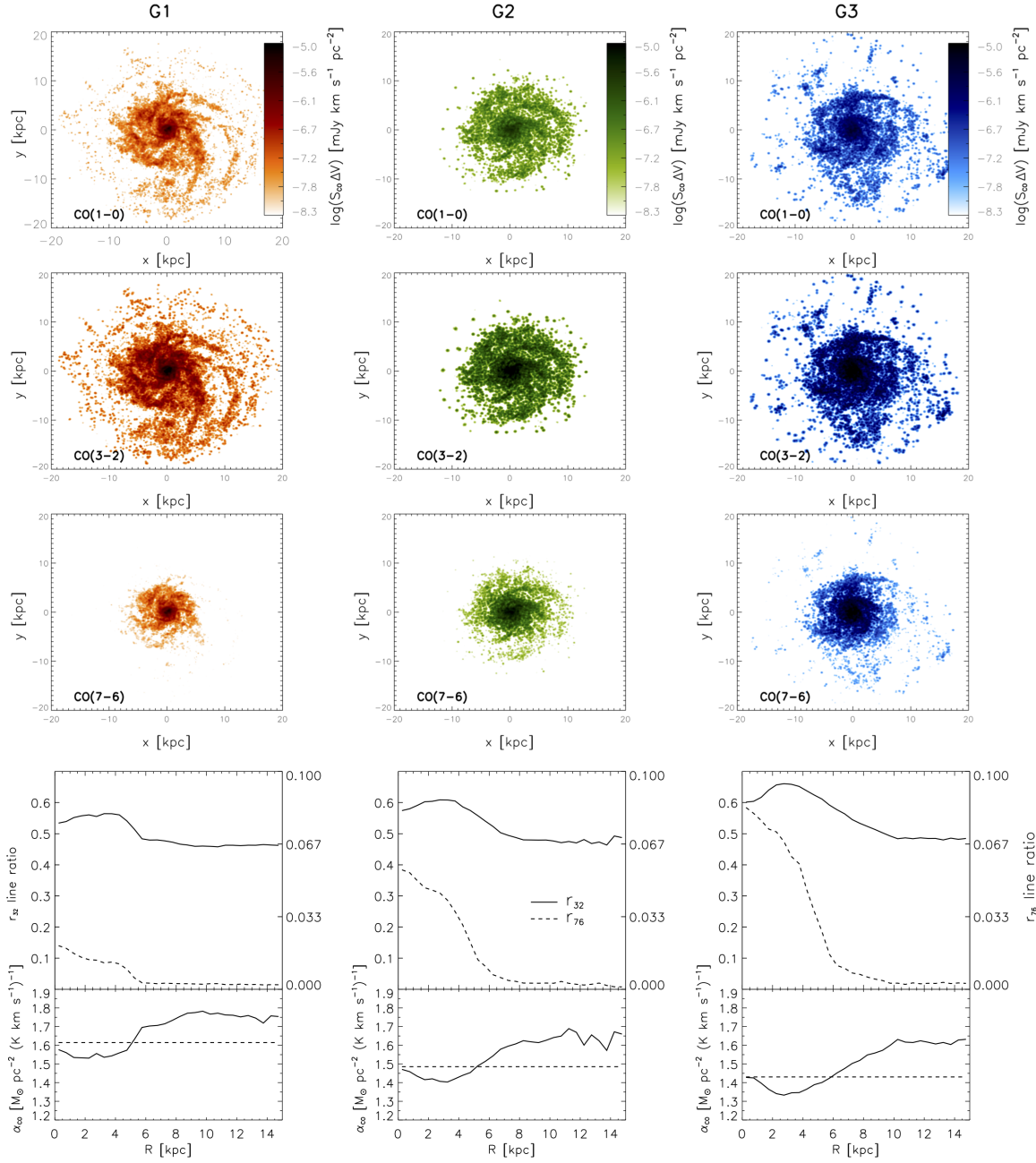


**Figure 9.** The top three rows show the moment zero maps of the CO(1-0), CO(3-2) and CO(7-6) emission from G1, G2 and G3. The CO maps have been smoothed using a circular Gaussian with full width at half maximum (FWHM) of 3 pixels corresponding to 0.24 kpc, and as with the SPH and molecular gas surface density maps, a logarithmic scale has been applied in order to better display extended emission. The bottom row shows the azimuthally averaged CO 3-2/1-0 and 7-6/1-0 brightness temperature line ratios (denoted  $r_{32}$  and  $r_{76}$ , respectively) as functions of projected radius for each of the three galaxies. A radial bin-size of 0.5 kpc was used. Also shown are the azimuthally averaged radial profiles of CO-to-H<sub>2</sub> conversion factor  $\alpha_{\text{CO}}(R) = \Sigma_{\text{H}_2}/I_{\text{CO}(1-0)}$  in units of  $\text{M}_{\odot} \text{ pc}^{-2} (\text{K km s}^{-1})^{-1}$  with a dashed line indicating the global  $\alpha_{\text{CO}}$  factor.

for nearby spirals in the work of Leroy et al. (2008)<sup>3</sup>. The radially binned  $\Sigma_{\text{mol}}$  reaches  $\sim 800 - 1000 \text{ M}_{\odot} \text{ pc}^{-2}$  in the

<sup>3</sup> The H<sub>2</sub> surface density maps in Fig. 8 are averaged over areas  $80 \times 80 \text{ pc}$  in size, and therefore give higher peak surface densities than the radial profiles which are averaged over  $\sim 0.5 \text{ kpc}$  wide annuli.

central regions of our simulated galaxies, which is comparable to observational estimates of  $\Sigma_{\text{mol}}$  (of several  $100 \text{ M}_{\odot} \text{ pc}^{-2}$ ) towards the centres of nearby spirals (Leroy et al. 2008). In all three galaxies, the H I + H II surface density dips within the central  $\sim 1 - 2 \text{ kpc}$ , coinciding with a strong peak in  $\Sigma_{\text{mol}}$ . Thus, despite the marked increase in the FUV radiation field towards the centre (the radial profile of  $G'_0$  is

shown as dash-dotted line in Figure 8), the formation of  $\text{H}_2$  driven by the increase in gas pressure is able to overcome photo-dissociative destruction of  $\text{H}_2$  by FUV photons. The central  $\text{H}_2$  surface densities are similar for all galaxies and is a direct consequence of very similar SPH gas surface densities in the centre combined with molecular gas mass fractions approaching 1. From  $R \sim 2 \text{ kpc}$  and out to  $\sim 10 \text{ kpc}$ , the  $\text{HI} + \text{HII}$  surface density remains roughly constant with values of  $\sim 40$ ,  $\sim 70$  and  $\sim 100 \text{ M}_\odot \text{ pc}^{-2}$  for G1, G2 and G3, respectively.

Radial profiles of the  $\text{HI}$  and molecular gas surface density that are qualitatively very similar to our simulations have been observed in several nearby star-forming disk galaxies (e.g., Leroy et al. 2008; Bigiel et al. 2008). In local galaxies, however, the  $\text{HI}$  surface density, including helium, rarely exceeds  $\sim 10 \text{ M}_\odot \text{ pc}^{-2}$ , while in our simulations we find  $\text{HI} + \text{HII}$  surface densities that are  $4 - 10 \times$  higher, indicating that there is a substantial fraction of ionised gas in our model galaxies.

#### 4.2 CO line emission maps and resolved excitation conditions

Moment zero maps of the  $\text{CO}(1-0)$ ,  $\text{CO}(3-2)$  and  $\text{CO}(7-6)$  emission from G1, G2 and G3 are shown in Figure 9. Comparing with the  $\text{H}_2$  surface density maps in Figure 8, both the  $\text{CO}(1-0)$  and  $\text{CO}(3-2)$  emission are seen to trace the  $\text{H}_2$  gas distribution well, while the  $\text{CO}(7-6)$  emission is restricted to the central  $\sim 7 \text{ kpc}$  of the galaxies.

Also shown in Figure 9 (bottom row) are the azimuthally averaged  $\text{CO } 3-2/1-0$  and  $7-6/1-0$  brightness temperature line ratios (denoted  $r_{32}$  and  $r_{76}$ , respectively) as a function of radius for G1, G2 and G3. The profiles show that the gas is clearly more excited in the central  $\sim 5 \text{ kpc}$ , where typical values of  $r_{32}$  and  $r_{76}$  are  $\sim 0.55 - 0.65$  and  $\sim 0.02 - 0.08$ , respectively, compared to  $r_{32} \sim 0.5$  and  $r_{76} < 0.01$  further out in the disk. This radial behaviour of the line ratios does not reflect the  $\text{H}_2$  gas surface density, which peaks towards the centre rather than flattens, and gradually trails off out to  $R \sim 12 \text{ kpc}$  instead of dropping sharply at  $R \sim 4 - 6 \text{ kpc}$  (Figure 9). Rather,  $r_{32}$  and  $r_{76}$  seem to follow closely the behaviour of  $G'_0$  (and thus  $\zeta_{\text{CR}}$ ), which makes sense since  $G'_0$  and  $\zeta_{\text{CR}}$  are the most important factors for the internal GMC temperature distribution (Figure C2). The central values for  $r_{32}$  and  $r_{76}$  increase when going from G1 to G3, as expected from the elevated levels of star formation density (and of  $G'_0$  and  $\zeta_{\text{CR}}$ , accordingly) towards the centre. Beyond  $\sim 6 \text{ kpc}$  the line ratios are constant ( $\sim 0.5$  and  $< 0.01$ ) and the same for all three galaxies, due to relatively similar FUV fields here.

At high- $z$ , resolved observations of single CO lines are starting to appear (e.g. Genzel et al. 2013; Hodge et al. 2014), but since resolved excitation studies using multiple lines have so far not been obtained, we instead compare our results to local quiescent and extreme galaxies. The increase in  $r_{32}$  towards the centres, are in agreement with observations of nearby galaxies as those carried out by Dumke (2000). Geach & Papadopoulos (2012) modeled two extreme cases of gas conditions, and found that while  $r_{32}$  might only be  $\sim 0.13$  in quiescent environments, it is typically  $\sim 0.88$  in denser gas. Mao et al. (2010) observed 125 nearby galaxies of different types and found  $r_{32}$  to be  $0.61 \pm 0.16$  in normal

galaxies, but  $> 0.89$  in starbursts and (U)LIRGs. Iono et al. (2009) and Papadopoulos et al. (2012) finds slightly lower  $r_{32}$  in their samples of (U)LIRGs, with mean values of  $0.48 \pm 0.26$  and  $0.67 \pm 0.62$  respectively. In light of these observations, the  $r_{32}$  radial profiles of our model galaxies, suggest a denser, ULIRG-like environment in the central ( $R < 5 \text{ kpc}$ ) region together with a more quiescent and diffuse gas phase further out in the disk of  $z = 2$  normal star-forming galaxies.

#### 4.3 The CO-to- $\text{H}_2$ conversion factor

The CO-to- $\text{H}_2$  conversion factor ( $\alpha_{\text{CO}}$ ) connects  $\text{CO}(1-0)$  line luminosity (in surface brightness temperature units) with the molecular gas mass ( $M_{\text{mol}}$ ) as follows:

$$\alpha_{\text{CO}} = \frac{M_{\text{mol}}}{L'_{\text{CO}(1-0)}}, \quad (16)$$

From the  $\text{CO}(1-0)$  surface brightness and  $\text{H}_2$  surface density maps of our model galaxies, we calculate  $\alpha_{\text{CO}}$  in radial bins surrounding the galaxy centres (Figure 9). The resulting radial  $\alpha_{\text{CO}}$  factors for our model galaxies lie in the range of  $\sim 3 - 4 \text{ M}_\odot \text{ pc}^{-2} (\text{K km s}^{-1})^{-1}$ , and show a clear transition from lower  $\alpha_{\text{CO}}$ -values inside the central  $R \sim 5 \text{ kpc}$  to higher values at  $R \gtrsim 6 \text{ kpc}$ . The drop in  $\alpha_{\text{CO}}$  from the disk average to the central value is about a factor  $\sim 1.6 - 1.7$ , similar to the drop in observed  $\alpha_{\text{CO}}$  profiles. Recently, Blanc et al. (2013) measured a drop in  $\alpha_{\text{CO}}$  by a factor of two when going from  $R \sim 7 \text{ kpc}$  to the centre of the Sc galaxy NGC 628, by using a constant gas depletion timescale in order to convert SFR surface densities into gas masses. Similarly, Sandstrom et al. (2013) found a drop by a factor of on average  $\sim 2$  from  $\alpha_{\text{CO}}$  averaged across the galaxy disks to  $\alpha_{\text{CO}}$  of the central  $R \leq 1 \text{ kpc}$  in 26 nearby spiral galaxies, by converting inferred dust masses into gas masses.

One could expect  $\alpha_{\text{CO}}$  to be correlated with  $Z'$ , as higher metallicity means higher C and O abundances as well as more dust that help shielding  $\text{H}_2$  formation sites from FUV radiation, and thereby increase the amount of CO, possibly lowering  $\alpha_{\text{CO}}$ . On the other hand, although a higher FUV field leads to more ionization and photo-dissociation, it also increases the gas temperatures, which translates into more excited CO molecules and again a lower  $\alpha_{\text{CO}}$  factor. Comparison of the  $\alpha_{\text{CO}}$  radial profiles with those of  $G'_0$  and  $Z'$  in the bottom panel of Figure 8, suggests that the transition in  $\alpha_{\text{CO}}$  is caused by a change in  $G'_0$  rather than a change in  $Z'$ , since  $\alpha_{\text{CO}}$  and  $G'_0$  generally start to drop at around  $R \sim 6 \text{ kpc}$  while  $Z'$  already drops drastically at  $1 \text{ kpc}$  from the centre. Our modeling therefore implies that  $\alpha_{\text{CO}}$  is controlled by  $G'_0$  rather than  $Z'$  in normal star-forming galaxies at  $z \sim 2$ , in agreement with the observations by Sandstrom et al. (2013) who do not find a strong correlation with  $Z'$ .

From the total molecular gas masses and  $\text{CO}(1-0)$  luminosities of our galaxies, we derive their global  $\alpha_{\text{CO}}$  factors. this gives global values of  $\alpha_{\text{CO}} = 1.6, 1.5$  and  $1.4 \text{ M}_\odot \text{ pc}^{-2} (\text{K km s}^{-1})^{-1}$  for G1, G2 and G3, respectively (In Section 5 we investigate the effect on  $\alpha_{\text{CO}}$  of different prescriptions for the GMC modeling, but for now stick to the default choices as specified above). These values are lower (by a factor  $\sim 3$ ) than the global MW value of  $\alpha_{\text{CO,MW}} \simeq 4.4 \pm 0.9 \text{ M}_\odot \text{ pc}^{-2} (\text{K km s}^{-1})^{-1}$ , calibrated from dynamical, dust, and  $\gamma$ -ray studies (e.g., Strong & Mattox 1996; Dame et al. 2001; Pineda et al. 2008), but closer to the typical

mergers/starburst  $\alpha_{\text{CO}}$ -values ( $\sim 0.2 \times \alpha_{\text{CO,MW}}$ ) inferred from CO dynamical studies of local ULIRGs (e.g., Solomon et al. 1997; Downes & Solomon 1998; Bryant & Scoville 1999) and  $z \sim 2$  SMGs (e.g., Tacconi et al. 2008). Our  $\alpha_{\text{CO}}$ -values are also below those inferred from dynamical modeling of  $z \sim 1.5$  BzKs ( $\alpha_{\text{CO}} = 3.6 \pm 0.8 \text{ M}_{\odot} \text{ pc}^{-2} (\text{K km s}^{-1})^{-1}$ ; Daddi et al. 2010).

On the other hand, the  $\alpha_{\text{CO}}$  factors of the  $z \sim 1 - 1.3$  star-forming galaxies studied by Magnelli et al. (2012) occupy the same region of the  $M_*$ -SFR plan as our model galaxies, but have  $\alpha_{\text{CO}}$  factors at least a factor  $\sim 6$  higher. Their  $\alpha_{\text{CO}}$  are  $\sim 5 - 20 \text{ M}_{\odot} \text{ pc}^{-2} (\text{K km s}^{-1})^{-1}$  when converting dust masses to gas masses using a metallicity-dependent gas-to-dust ratio, and Magnelli et al. (2012) further find that the same galaxies have relatively low dust temperatures of  $\lesssim 28 \text{ K}$  compared to the galaxies further above the main sequence of Rodighiero et al. (2010). The fact that the main-sequence galaxies of Magnelli et al. (2012) are all of near-solar metallicity as ours, cf. Table 1, suggests that other factors, such as dust temperature caused by strong FUV radiation, can be more important than metallicity in regulating  $\alpha_{\text{CO}}$ , in line with our study of the  $\alpha_{\text{CO}}$  radial profiles.

#### 4.4 Global CO line luminosities and spectral line energy distributions

The global CO SLEDs of G1, G2 and G3 are shown in Figure 10 in three different incarnations: 1) total CO line luminosities ( $L'_{\text{CO},J-1}$ ), 2) brightness temperature ratios ( $T_{\text{B,CO},J-1}/T_{\text{B,CO},1,0} = L'_{\text{CO},J-1}/L'_{\text{CO},1,0}$ ) and 3) line intensity ratios ( $I_{\text{CO},J-1}/I_{\text{CO},1,0} = L'_{\text{CO},J-1}/L'_{\text{CO},1,0} \times (\nu_{\text{CO},J-1}/\nu_{\text{CO},1,0})^2$ ). In Figure 10 we have also compiled all relevant CO observations of normal star-forming galaxies at  $z \sim 1 - 3$  to date in order to facilitate a comparison with our simulated CO SLEDs of such galaxies. Samples are the same as in Figure 2, but including an additional 7 star-forming galaxies (SFGs) at  $z \sim 1.2$  (Magnelli et al. 2012) and another 39 SFGs at  $z \sim 1 - 1.5$  (Tacconi et al. 2013). The first sample of galaxies are all detected in CO(2-1) as well as in *Herschel*/PACS bands, and have  $\log M_* = 10.36 - 11.31$  and  $\text{SFR} \sim 29 - 74 \text{ M}_{\odot} \text{ yr}^{-1}$ . The sample from Tacconi et al. (2013) comes from the Extended Growth Strip International Survey (EGS), is covered by the CANDELS and 3D-HST programs ( $J - H$  bands and  $\text{H}\alpha$  respectively), and has  $\log M_* = 10.40 - 11.23$  and  $\text{SFR} \sim 28 - 630 \text{ M}_{\odot} \text{ yr}^{-1}$ .

First, we compare the total CO(3-2) luminosities of our model galaxies with those of the  $z \sim 2 - 2.5$  BX/BM galaxies of Tacconi et al. (2013), which are not only closest in redshift to our model galaxies but also occupy the same region of the SFR- $M_*$  plane (see Figure 2). We find that G2 and G3, the two most massive ( $M_* > 10^{11} \text{ M}_{\odot}$ ) and star-forming ( $\text{SFR} \gtrsim 80 \text{ M}_{\odot} \text{ yr}^{-1}$ ) galaxies of our simulations, have CO(3-2) luminosities of  $\sim 0.7 - 1 \times 10^{10} \text{ K km s}^{-1} \text{ pc}^2$ , which is in the range of CO(3-2) luminosities of the BX/BM galaxies at an average of  $\sim 1.2 \pm 0.9 \times 10^{10} \text{ K km s}^{-1} \text{ pc}^2$ . The more quiescent G1 is about a factor 4 below the average  $L'_{\text{CO}(3-2)}$  of BX/BM galaxies, and the offset from the BzK galaxies is even bigger. Our G2 and G3 simulations, however, are able to reproduce the CO luminosities of the  $z \simeq 1 - 1.5$  SFGs observed by Magnelli et al. (2012) and Tacconi et al. (2013), which span a range in CO(2-1) and CO(3-2) luminosities

of  $(3.6 - 12.5) \times 10^9$  and  $(1.4 - 41.3) \times 10^9 \text{ K km s}^{-1} \text{ pc}^2$ , respectively. In general, the BzK galaxies are more luminous than our model galaxies, with the exception of BzK-16000 at a SFR of  $152 \text{ M}_{\odot} \text{ yr}^{-1}$  only slightly above our G2 model galaxy ( $142 \text{ M}_{\odot} \text{ yr}^{-1}$ ). As mentioned in Section 4.1, the molecular gas mass fractions of our galaxies is about a factor 6 below the mean of the observed galaxies at  $z \sim 1 - 2.5$  with which we compare, and we propose this as the main reason for the comparatively low CO luminosities.

Differences in the global CO excitation conditions between G1, G2 and G3 are best seen in the CO(1-0) normalized luminosity (and intensity) ratios, i.e., middle (and bottom) panel in Figure 10). The CO SLEDs of all three galaxies follow each other quite closely up to the  $J = 3 - 2$  transition where the SLEDs all peak; at  $3 < J_{\text{up}} < 7$  the SLEDs gradually diverge. While the metallicity distributions in G1, G2 and G3 are similar (see Figure C1), the rise in  $G'_0$  presents a likely cause to the increasing high- $J$  flux when going from G1 to G3, as higher  $G'_0$  leads to more flux primarily in the  $J > 4$  transitions (see Figure C3).

Our simulated galaxies are seen to have CO 2-1/1-0, 3-2/1-0, and 5-4/1-0 brightness temperature ratios of  $r_{21} \simeq 1$ ,  $r_{32} \simeq 0.55$ , and  $r_{54} \simeq 0.15$ , respectively. The first two ratios compare extremely well with the line ratios measured for BzK-4171 and BzK-21000, i.e.,  $r_{21} \simeq 0.9 - 1$ , and  $r_{32} \simeq 0.5 - 0.6$  (Dannerbauer et al. 2009; Aravena et al. 2010; Daddi et al. 2010, 2014), and suggest that our simulations are able to emulate the typical gas excitation conditions responsible for the excitation of the low- $J$  lines in normal  $z \sim 1 - 3$  SFGs. In contrast,  $r_{54} = 0.3 - 0.4$  observed in BzK-4171 and BzK-21000 (Daddi et al. 2014), is nearly  $2\times$  higher than our model predictions. Daddi et al. (2014) argue that this is evidence for a component of denser and possibly warmer molecular gas, not probed by the low- $J$  lines. In this picture, we would expect CO(4-3) to probe both the cold, low-excitation gas as well as the dense and possibly warm star-forming gas traced by the CO(5-4) line; and we would expect CO(6-5) to be arising purely from this more highly excited phase and thus departing even further from our models.

However, significant scatter in the CO line ratios of main-sequence galaxies is to be expected, as demonstrated by the significantly lower line ratios observed towards BzK-16000:  $r_{21} \simeq 0.4$ ,  $r_{32} \simeq 0.3$ , and  $r_{54} \simeq 0.1$  (Aravena et al. 2010; Daddi et al. 2010, 2014) and, in fact, the average  $r_{54}$  for all three BzK galaxies above ( $\simeq 0.2$ ; Daddi et al. (2014)) is consistent with our models. It may be that G2 and G3, and perhaps even G1, are more consistent with the CO SLEDs of the bulk  $z \sim 1 - 3$  main-sequence galaxies. We stress, that to date, no  $z \sim 1 - 3$  main sequence galaxies have been observed in the  $J = 4 - 3$  nor the  $6 - 5$  transitions, and observations of these lines, along with low- and high- $J$  lines in many more BzK and main-sequence  $z \simeq 1 - 3$  galaxies are needed in order to fully delineate the global CO SLEDs in a statistically robust way.

## 5 TESTING DIFFERENT ISM MODELS

In this section we investigate the effects on our simulation results when adopting i) a shallower GMC mass spectrum slope of  $\beta = 1.5$ , ii) a steeper GMC density profile, i.e., a



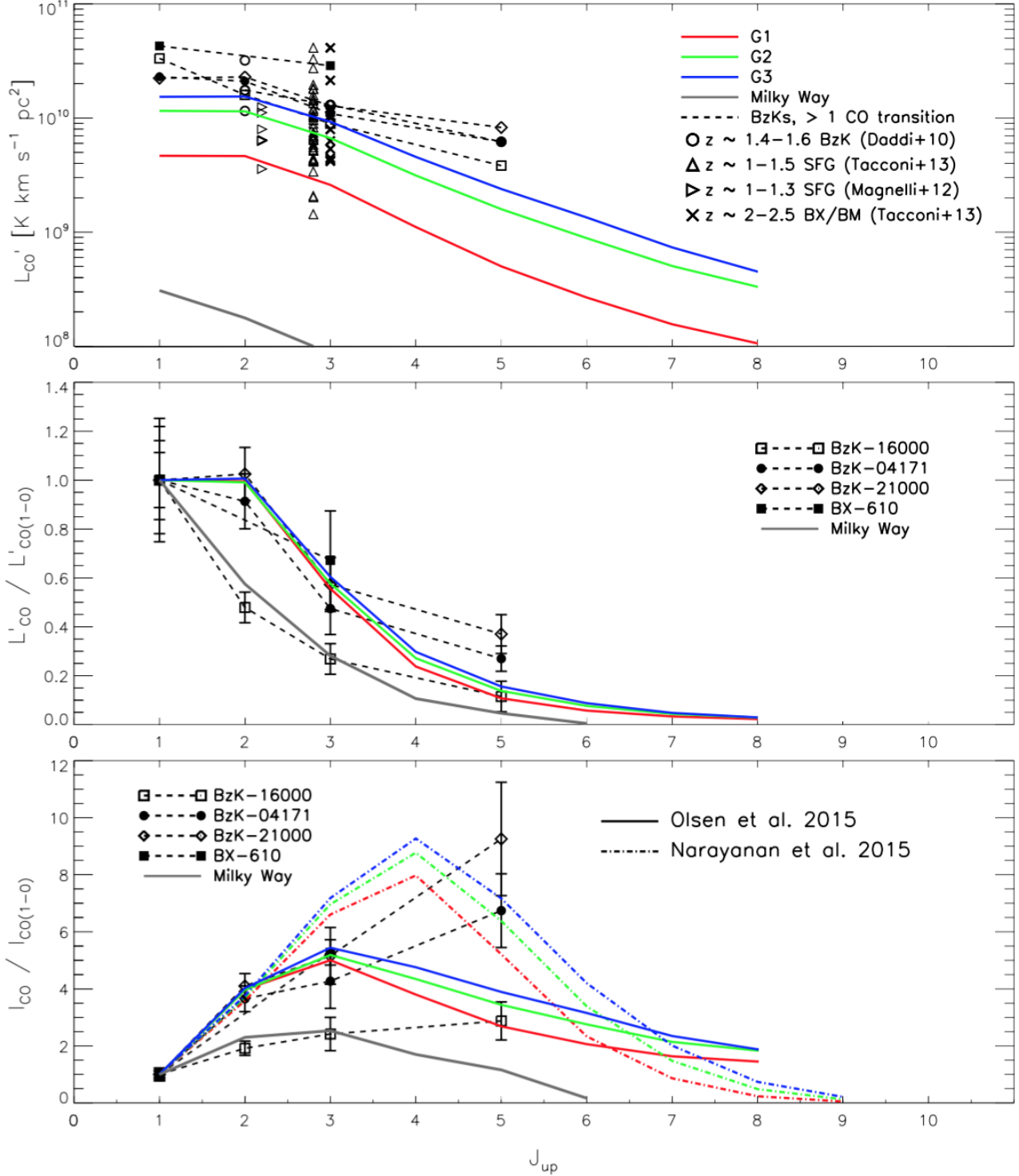


**Figure 10.** Global CO SLEDs of our three model galaxies G1, G2 and G3 shown as red, green and blue solid curves, respectively. The SLEDs are given as absolute line luminosities in units of  $\text{K km s}^{-1} \text{ pc}^2$  (top panel), as brightness temperature ratios normalized to the CO(1–0) transition (middle panel), and as velocity-integrated intensity ratios normalized to CO(1–0) (bottom panel). The model CO SLEDs are compared with observations of  $z \sim 1.4 - 1.6$  BzK galaxies (CO(1–0) and CO(2–1); Dannerbauer et al. 2009; Daddi et al. 2010, 2014; Aravena et al. 2010, 2014),  $z \sim 1 - 1.5$  star-forming galaxies (CO(3–2); empty triangles; Tacconi et al. 2013),  $z \sim 1 - 1.3$  star-forming galaxies (CO(1–0) and CO(2–1); rightfacing triangles; Magnelli et al. 2012), and  $z \sim 2 - 2.5$  BX/BM galaxies (CO(3–2); crosses; Tacconi et al. 2013). Also shown is the global CO SLED of the MW (grey line; Fixsen et al. 1999). Three BzK galaxies (BzK–16000, BzK–4171, and BzK–21000) have been observed in CO(1–0) and at least one additional transition to date, and are highlighted by connecting dashed lines. Also shown in the bottom panel, with dash-dotted lines, are the line ratio predictions of Narayanan & Krumholz (2014) (D14), calculated for the  $\Sigma_{\text{SFR}}$  of our galaxies (see text).

Plummer profile exponent of  $-7/2$ , and iii) GMC model grid that includes a the external cloud pressure,  $P_{\text{ext}}$ , as a fourth parameter. In order to carry out option iii), the GMC model grid was produced for pressures of  $P_{\text{ext}}/k_B = 10^4 \text{ cm}^{-3} \text{ K}$  (default),  $10^{5.5} \text{ cm}^{-3} \text{ K}$  and  $10^{6.5} \text{ cm}^{-3} \text{ K}$ , allowing for a look-up table of CO SLEDs in  $(G'_0, m_{\text{GMC}}, Z', P_{\text{ext}})$  parameter space. We examine the effects that options i)-iii) have on the global CO SLED of galaxy G2 (Figure 11) and how combinations of option i) and ii) change the values of the global CO-to- $\text{H}_2$  conversion factor (Table 3). Also, we show the impact changes ii) and iii) have on the CO SLEDs of the individual GMC grid models in Figures C4 and C5.

Changing the GMC mass spectrum from  $\beta = 1.8$  to 1.5 leaves the CO SLED virtually unchanged (dotted and dot-dashed curves in the top panel of Figure 11) with only a marginal increase in the line ratio for  $J_{\text{up}} \geq 4$ .

Adopting the modified Plummer density profile with a power-law exponent of  $-7/2$  instead of  $-5/2$  leads to significantly higher line intensity ratios (i.e.,  $I_{\text{CO}}/I_{\text{CO}(1-0)}$ ) for  $J_{\text{up}} \geq 3$  (see dotted vs. dashed curve and dot-dashed vs. solid curves in top panel of Figure 11.) This increase in line intensity comes from an increase in central densities, as shown in Fig. 7, leading to the excitation of higher  $J$  lines.

Including external pressures of  $P_{\text{ext}}/k_B = 10^{5.5} \text{ cm}^{-3} \text{ K}$  and  $10^{6.5} \text{ cm}^{-3} \text{ K}$  to the GMC model grid, leads to more compact GMCs with decreased velocity dispersions (see eqs. 9 and 10), both of which act to suppress the CO luminosity at high transitions via increased optical depths. The effect of employing these high pressure grids on the global CO SLED, is depicted in the bottom panel of Figure 11. The most noticeable change in the global CO SLEDs is a steeper decline at high ( $J_{\text{up}} \geq 4$ ) transitions.

In Table 3 we compare the global  $\alpha_{\text{CO}}$  factors pertaining to different choices for the GMC mass spectrum and density profile. As evident from Fig. C3, higher GMC mass leads to an increase in  $\text{CO}(1-0)$  luminosity for individual GMC models. Using the shallower slope of  $\beta = 1.5$  for the GMC mass spectrum results in an increase in the fraction of massive GMCs at the expense of low-mass GMCs. This fractional increase in massive GMCs produces a smaller  $\text{CO}(1-0)$  luminosity contribution than the low-mass GMCs removed, and the net effect of adopting  $\beta = 1.5$  is therefore a reduction in the global  $\text{CO}(1-0)$  luminosity. In terms of  $\alpha_{\text{CO}}$ , changing  $\beta$  from 1.8 to 1.5 therefore leads to the slightly larger  $\alpha_{\text{CO}}$  factors provided in Table 3. Similarly, despite the increasing line ratios at  $J_{\text{up}} \geq 3$ , a steeper GMC density profile decreases the  $\text{CO}(1-0)$  luminosity of our GMC models as evident in Fig. C4, thereby increasing  $\alpha_{\text{CO}}$ . In both cases though,  $\alpha_{\text{CO}}$  is still kept below the standard MW-value. From the numbers in Table 3,  $\alpha_{\text{CO}}$  for normal star-forming  $z \sim 2$  galaxies is predicted to lie in the range  $\sim 1.4 - 4.0 \text{ M}_{\odot} \text{ pc}^{-2} (\text{K km s}^{-1})^{-1}$  or  $\sim 0.3 - 0.9$  times the MW value.

## 6 COMPARISON WITH OTHER MODELS

SÍGAME relies on subgrid physics to describe the molecular gas in high- $z$  galaxies, e.g., cloud masses, their density and temperature structure etc. It is assumed that the scaling

**Table 3.** The average of the global  $\text{H}_2$ -to-CO conversion factors (in units of  $\text{M}_{\odot}/(\text{K km s}^{-1} \text{ pc}^2)$ ) for G1, G2, and G3, for for different ISM models. The pressure has been kept fixed at  $P_{\text{ext}}/k_B = 10^4 \text{ cm}^{-3} \text{ K}$ .

	$\beta = 1.8$ (MW)	$\beta = 1.5$ (vir)
Plummer profile	$1.51 \pm 0.10$	$1.47 \pm 0.10$
Modified Plummer profile	$3.62 \pm 0.44$	$3.45 \pm 0.46$

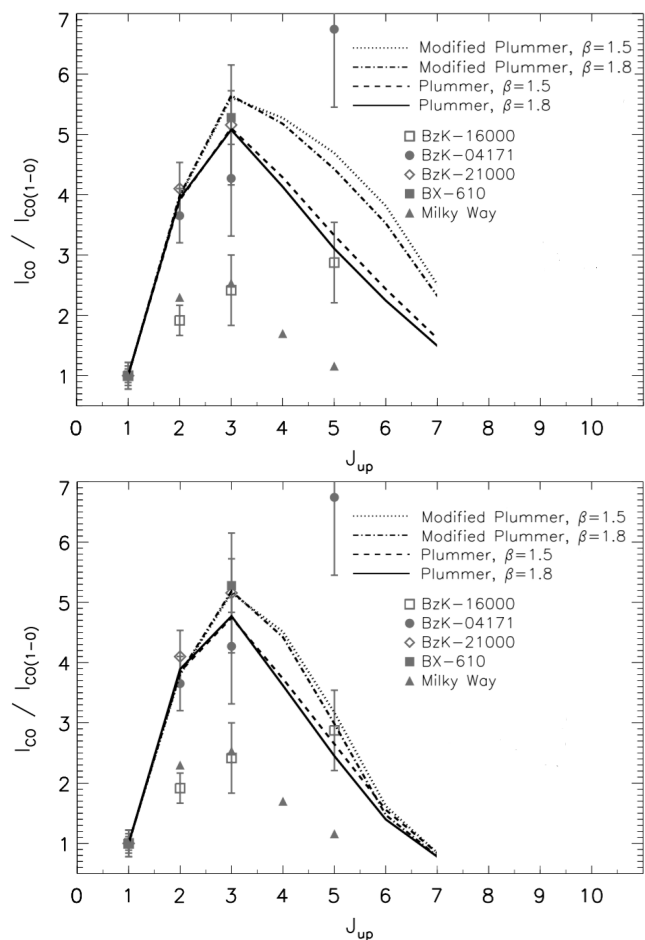


**Figure 11.** Global CO SLEDs of our model galaxy G2 for different choices of ISM prescriptions. *Top:* For a pressure fixed of  $10^4 \text{ cm}^{-3} \text{ K}$ . *Bottom:* Using the  $P_{\text{ext}}$  as a fourth parameter in the GMC model grid (see Section 3.4.4).

and thermal balance equations that have been established and calibrated to GMC complexes in our own Galaxy can be extrapolated to the ISM conditions in high- $z$  galaxies. Similarly, all other numerical simulations made to date of the molecular gas in galaxies and their CO line emission rely to smaller or larger degree on subgrid physics (e.g., Narayanan et al. 2006; Pelupessy et al. 2006; Greve & Sommer-Larsen 2008; Christensen et al. 2012; Lagos et al. 2012; Muñoz & Furlanetto 2014; Narayanan & Krumholz 2014; Lagos et al. 2012; Popping et al. 2014). In this section we will highlight and discuss some of the differences in the subgrid physics between SÍGAME and other simulations.

First, however, we compare the SÍGAME CO SLEDs of

G1, G2, and G3 with those predicted by other CO emission simulations of similar main-sequence galaxies. A direct comparison with **SÍGAME** can be made in the case of the models presented by Narayanan & Krumholz (2014), where the global CO SLED is parametrised as a function of the SFR surface density ( $\Sigma_{\text{SFR}}$ ). Using the SFR surface densities (averaged over the inner 5 kpc) of our model galaxies, the corresponding CO SLEDs inferred from the Narayanan & Krumholz (2014) parametrisation are shown as dash-dotted lines in Figure 10 (bottom panel). The SLEDs of Narayanan & Krumholz (2014) all peak at  $J = 4 - 3$  and not  $3 - 2$  as our SLEDs, and the line flux ratios are significantly higher at transitions between  $J = 3 - 2$  and  $6 - 5$ . While a direct comparison is not possible, we note that (Lagos et al. 2012) provide CO SLED predictions for  $z = 2$  main-sequence galaxies are in agreement with those of Narayanan & Krumholz (2014), when comparing galaxies of similar infrared luminosities as ours. Converting SFRs to infrared luminosities with the Kennicutt (1998) conversion factor adapted to a Chabrier IMF,  $L_{\text{IR}}/L_{\odot} = \text{SFR}/[\text{M}_{\odot} \text{ yr}^{-1}] \times 10^{10}$  (see Daddi et al. 2010), our simulated galaxies G1, G2 and G3 have  $L_{\text{IR}}$  of 0.40, 0.80 and  $1.4 \times 10^{12} L_{\odot}$ , respectively, which is in the bottom of the range typically observed for BzK galaxies ( $L_{\text{IR}}$  from 0.6 to  $4.0 \times 10^{12} L_{\odot}$ ; Daddi et al. 2010). For galaxies with infrared luminosities  $L_{\text{IR}} \sim 10^{11.25} - 10^{12} L_{\odot}$ , corresponding to the range of  $L_{\text{IR}}$  in our simulated galaxies, Lagos et al. (2012) predict CO SLEDs that peak in the CO(4–3) transition, that is, again implying slightly more excited gas than **SÍGAME** does. Popping et al. (2014) find an interesting trend with redshift in their semi-analytical study of MS galaxies at  $z = 0, 1.2$  and 2; Galaxies with far-infrared (FIR) luminosities of  $\log(L_{\text{FIR}}/L_{\odot}) = 11 - 12$  peak at CO(3–2) or CO(4–3) at  $z = 0$ , but at CO(6–5) at  $z = 2$ . Our galaxies lie in the same FIR luminosity range ( $\log(L_{\text{FIR}}/L_{\odot}) = 11.4 - 11.9$  when converting  $L_{\text{IR}}$  to  $L_{\text{FIR}}$  by dividing by 1.7; Chapman et al. 2000), but again **SÍGAME** predicts less excited gas when comparing to the  $z \sim 2$  MS galaxies of Popping et al. (2014).

#### • Implementation of $G'_0$ and $\zeta_{\text{CR}}$

**SÍGAME** stands out from most other simulations to date in the way the FUV radiation field and the CR flux that impinge on the molecular clouds are modelled and implemented. Most simulations adopt a fixed, galaxy-wide value of  $G'_0$  and  $\zeta_{\text{CR}}$ , scaled by the total SFR or average gas surface density across the galaxy (e.g., Lagos et al. 2012; Narayanan & Krumholz 2014). **SÍGAME** refines this scheme by determining a spatially varying  $G'_0$  (and  $\zeta_{\text{CR}}$ ) set by the local SFRD, as described in Section 3.3. By doing so, we ensure that the molecular gas in our simulations is calorimetrically coupled to the star formation in their vicinity. If we adopt the method of Narayanan & Krumholz (2014) and calculate a global value for  $G'_0$  by calibrating to the MW value, using  $\text{SFR}_{\text{MW}} = 2 \text{ M}_{\odot} \text{ yr}^{-1}$  and  $G'_{0,\text{MW}} = 0.6 \text{ Habing}$ , our galaxies would have  $G'_0$  ranging from about 12 to 42, whereas, with the SFR surface density scaling of Lagos et al. (2012), global  $G'_0$  values would lie between about 6 and 9. For comparison, the locally determined  $G'_0$  in our model galaxies spans a larger range from 0.3 to 27 (see Figure C1). Narayanan & Krumholz (2014) determines the global value of  $\zeta_{\text{CR}}$  as  $2 \times 10^{-17} \text{ Z}' \text{ s}^{-1}$ , corresponding to values of  $3.7 - 6.2 \times 10^{-17} \text{ s}^{-1}$  in our model galaxies, when using the mass-weighted mean of  $Z'$  in each

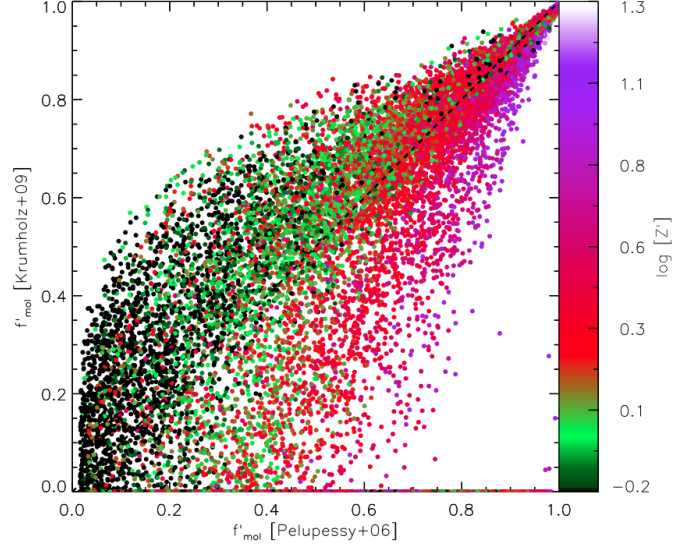


**Figure 12.** Comparison of two methods for calculating the molecular gas mass fraction,  $f'_{\text{mol}}$ , of SPH particles in G1: That of Pelupessy et al. (2006) with external cloud pressure derived from hydrostatic mid-plane equilibrium as done in this work (abscissa) and that of Krumholz et al. (2009) (ordinate) used by e.g., Narayanan & Krumholz (2014), color-coded by metallicity.

galaxy. Typical values adopted in studies of ISM conditions are around  $(1 - 2) \times 10^{-17} \text{ s}^{-1}$  (Wolfire et al. 2010; Glover & Clark 2012), but again, the local values of  $\zeta_{\text{CR}}$  in our galaxies span a larger range, from  $1.3 \times 10^{-17}$  to  $1.3 \times 10^{-15} \text{ s}^{-1}$ .

#### • The molecular gas mass fraction

In **SÍGAME** the molecular gas mass fraction ( $f'_{\text{mol}}$ ) is calculated following the work by Pelupessy et al. (2006), in which  $f'_{\text{mol}}$  depends on temperature, metallicity, local FUV field, and boundary pressure on the gas cloud in question. Other methods exist, such as those of Blitz & Rosolowsky (2006) and Krumholz et al. (2009) (K09). Most recently, Narayanan & Krumholz (2014) applied the K09 model in order to derive the  $\text{H}_2$  gas mass, and we compare this method to that of Pelupessy et al. (2006) (P06), used by **SÍGAME**, in Figure 12. The gas surface density that enters in the K09 method was estimated within 1 kpc of each SPH particle, as used in our calculation of  $P_{\text{ext}}$  (see Section 3.3). Both methods produce higher  $f'_{\text{mol}}$  for increasingly more metal-rich gas, as expected since higher metallicity leads to more dust onto which the  $\text{H}_2$  molecules can form. As shown in Fig. 12, the two methods agree overall albeit with increasing scatter towards lower metallicity. For high metallicity, the P06 method tends to give larger values of  $f'_{\text{mol}}$  than the K09 method. This leads to systematically lower total molecular gas masses when using the method of K09 instead of P06. In particular, the molecular gas mass fractions,  $f_{\text{mol}} = M_{\text{mol}}/(M_{\star} + M_{\text{mol}})$ , of G1, G2 and G3 decrease from 8.5, 7.8 and 6.8 % to 9.8, 10.3 and 9.5 % respectively.

A common feature of the above  $\text{H I} \rightarrow \text{H}_2$  prescriptions is that they assume an instantaneous  $\text{H I}$  to  $\text{H}_2$  conversion, once the conditions for  $\text{H}_2$  formation are met. By actually incorporating their  $\text{H I} \rightarrow \text{H}_2$  subgrid model in an N-body/SPH dwarf galaxy simulation, Pelupessy et al. (2006)

find that typical timescales for  $\text{H}_2$  cloud formation are of order  $\sim 10^7$  yr. Such timescales are comparable to a wide variety of processes that can potentially alter or even fully disrupt typical molecular clouds, leading to the conclusion that modeling of the  $\text{H I} \rightarrow \text{H}_2$  transition should be time-dependent, in order to embrace such phenomena as clump-clump collisions and star formation, which can drive  $\text{H}_2$  formation in both directions. Relying on the findings of Narayanan et al. (2011) and Krumholz & Gnedin (2011), the static solution for  $\text{H}_2$  formation is a valid approximation for  $Z' > 0.01$ , which is the case for the three model galaxies studied here, but restricts SÍGAME to the domain of galaxies with at least  $Z' \sim 0.01$ .

#### • CO abundance

For the density of CO, we assumed that CO follows the structure of  $\text{H}_2$  gas, and adopted a constant Galactic abundance of  $[\text{CO}/\text{H}_2] = 2 \times 10^{-4}$ . In reality,  $\text{H}_2$  gas can self-shield better than the CO gas, creating an outer region or envelope of ‘CO-dark’ gas (Bolatto et al. 2008). Observations in the MW by Pineda et al. (2013) indicate that the amount of dark gas grows with decreasing metallicity and the resulting absence of CO molecules. By modeling a dynamically evolving ISM with cooling physics and chemistry incorporated on small scales, Smith et al. (2014) showed that in a typical MW-like disk of gas, the dark gas mass fraction,  $f_{\text{DG}}$ , defined as having  $W_{\text{CO}} < 0.1 \text{ K km s}^{-1}$ , is about 42%, but up to 62% in a radiation field ten times that of the solar neighbourhood. While Smith et al. (2014) kept metallicity constant throughout the disk, Wolfire et al. (2010) found  $f_{\text{DG}}$  values of about 0.5 – 0.7 for the low metallicity cases with  $Z' = 0.5$ , however using a 1D PDR model only. Recently, Bisbas et al. (2015) showed how relatively modest CR ionization rates of  $10 - 50 \times \zeta_{\text{CR,MW}}$  can effectively destroy most CO in GMCs. Such studies show, that  $[\text{CO}/\text{H}_2]$  is lower in regions of low metallicity and/or intense FUV fields, effectively leading to underestimates of the  $\alpha_{\text{CO}}$  conversion factor when not accounted for in models. Since in this paper we have restricted our simulations to main-sequence galaxies with solar or higher than solar metallicities, adopting a constant Galactic  $[\text{CO}/\text{H}_2]$  seems a reasonable choice, but see Lagos et al. (2012), Narayanan et al. (2012) and Narayanan & Krumholz (2014) for alternative approaches.

#### • GMC density and thermal structure

When solving for the temperature structure of each GMC, SÍGAME includes only the most dominant atomic and molecular species in terms of heating and cooling efficiencies. In this approximation, we also neglect X-ray irradiation and turbulence, leaving these for a future study. We have, however, checked our  $T_{\text{k}} - n_{\text{H}_2}$  curves in Figure C2 against those of Glover & Clark (2012), who performed time-resolved, high-resolution ( $\delta m \simeq 0.05 - 0.5 \text{ M}_{\odot}$ ) SPH simulations of individual FUV irradiated molecular clouds using a chemical network of 32 species (see their Figure 2). Overall, there is great similarity in the  $T_{\text{k}}$  vs.  $n_{\text{H}_2}$  behaviour of the two sets of simulations. This includes the same main trend of decreasing temperature with increasing hydrogen density, as well as the local increase in  $T_{\text{k}}$  at  $\sim 10^3 - 10^4 \text{ cm}^{-3}$  and the subsequent decrease to  $T_{\text{k}} < 10 \text{ K}$  at  $n_{\text{H}_2} > 10^{5.5} \text{ cm}^{-3}$ . Thus, our GMCs models, despite their simplified density profiles and chemistry, seem to agree well with much more detailed

simulations and we take this as an indication that they also mimic the conditions in real molecular clouds well.

## 7 SUMMARY

In this paper we have presented SÍGAME, a code that simulates the molecular line emission of galaxies via a detailed post-processing of the outputs from cosmological SPH simulations. A sequence of subgrid prescriptions are applied to a simulation snapshot in order to derive the molecular gas density and temperature from the SPH particle information such as SFR, gas density, temperature and metallicity. SÍGAME stands out from other methods of its kind by combining cosmological galaxy simulations with the following aspects:

#### (i) Local FUV field and cosmic ray ionization rate

In SÍGAME, the energetics of the ISM are driven by the local star formation rate density, which is what sets the local FUV and cosmic ray field, i.e.  $G'_0$  and  $\zeta_{\text{CR}}$  respectively, and thus the heating and ionization of the gas. Unlike other simulations, SÍGAME can therefore be used to study resolved properties within a galaxy, as for example line ratios and  $\alpha_{\text{CO}}$  factors.

#### (ii) Multiphase ISM

The partly ionised gas in the SPH simulation is first cooled down to a cold neutral phase by including only heating by cosmic rays, counter-balanced by cooling via metal line emission, recombination processes and free-free emission. In a second cooling step, SÍGAME determines the internal radial temperature profile of each GMC by considering cosmic ray heating and photo-electric heating by FUV photons as well as cooling by  $\text{H}_2$ , CO, OI, CII lines in addition to gas-dust interactions.

#### (iii) Radiative transfer on sub-parsec scales

We constructed a grid of GMC models that probe a large range in  $m_{\text{GMC}}$ ,  $Z'$  and  $G'_0$ . On each model, the novel radiative transfer code LIME was employed for determining the CO line emission, so that SÍGAME can interpolate in  $[m_{\text{GMC}}, Z', G'_0]$ -space and sum up the emission in several CO lines for an entire galaxy in a few minutes.

We have used SÍGAME to create line emission velocity-cubes of the full CO rotational ladder for three cosmological N-body/SPH simulations of massive ( $M_* \gtrsim 10^{10.5} \text{ M}_{\odot}$ ) main-sequence galaxies at  $z = 2$ .

Molecular gas is produced more efficiently towards the centre of each galaxy, and while H I surface gas densities (including helium) do not exceed  $\sim 100 \text{ M}_{\odot} \text{ pc}^{-2}$  anywhere in the disk, central molecular gas surface densities reach  $\sim 1000 \text{ M}_{\odot} \text{ pc}^{-2}$  on spatial scales of  $80 \text{ pc} \times 80 \text{ pc}$ , in good agreement with observations made at similar spatial resolution. This strong increase in molecular surface density is brought on by a similar increase in total gas surface density, overcoming the increase in photo-dissociating FUV field towards the centre of each galaxy.

Turning to the CO emission, the velocity-integrated moment 0 maps reveal distinct differences in the various transitions as molecular gas tracers. The morphology of molecular gas in our model galaxies is well reproduced in CO(1-0), but going to higher transitions, the region of CO emitting gas

shrinks towards the galaxy centres. The global CO SLEDs of our simulated galaxies all peak at  $J = 3 - 2$ , indicating a dominating low-excitation gas. Recent CO(5 - 4) observations of  $z \sim 1.5$  BzK galaxies seem to suggest that these galaxies actually peak at higher  $J$ , presenting an important test case that we will be following closely in the future in order to benchmark **SÍGAME** fully at  $z \sim 2$  before moving to e.g. higher redshifts. The CO(3 - 2) line luminosities of our model galaxies are within the range of corresponding observed samples at redshifts  $z \sim 1 - 2.5$ , however on the low side. In particular, the model galaxies are below or at the CO luminosities of BzK-selected galaxies of comparable mass and SFR but at  $z \sim 1.5$ . The low luminosities are most likely a consequence of molecular gas mass fractions in our galaxies about 6 times below the observed values in the star-forming galaxies at  $z = 1 - 2.5$  used to compare with.

Combining the derived H<sub>2</sub> gas masses with the CO(1 - 0) line emission found, we investigate local variations in the CO-H<sub>2</sub> conversion factor  $\alpha_{\text{CO}}$ . The radial  $\alpha_{\text{CO}}$  profiles all show a decrease towards the galaxy centres, dropping by a factor of  $\sim 1.6 - 1.7$  in the central  $R \leq 1$  kpc region compared to the disk average, and the main driver being the FUV field rather than a gradient in density or metallicity. Global  $\alpha_{\text{CO}}$  factors range from 1.4 to  $1.6 \text{ M}_{\odot} \text{ pc}^{-2} (\text{K km s}^{-1})^{-1}$  or about 0.3 times the MW value, but closer to values for  $z \sim 1.5$  normal star-forming galaxies identified with the BzK colour criteria.

The CO luminosity ratios of CO 3-2/1-0 and 7-6/1-0 ( $r_{32}$  and  $r_{76}$  respectively) drop off in radius about where the FUV radiation drops in intensity, and thus likely controlled by FUV field as  $\alpha_{\text{CO}}$ . The global ratios of  $r_{21} \simeq 1.4$  and  $r_{32} \simeq 0.7$  agree very well with observations of BzK galaxies, while the  $r_{54}$  of about 0.8 is low compared to recent observations in BzK-4171 and BzK-21000. However, more observations of  $J_{\text{up}} > 3$  lines towards high- $z$  main-sequence galaxies, such as the BzKs, are still needed in order to determine the turn-over in their CO SLEDs and better constrain the gas excitation.

Finally, we note that **SÍGAME** in principle is able to simulate the emission from a broad range of molecular and atomic lines in the far-IR/mm wavelength regime provided measured collision rates exist, such as those found in the LAMDA database<sup>4</sup>, are available. In the future, we aim to apply **SÍGAME** to a larger and more diverse sample of galaxies, possibly at higher redshift, and explore the emission from other important ISM diagnostic lines.

## ACKNOWLEDGMENTS

We are grateful to Inti Pelupessy for elaborations on his papers and help with the ionization fractions, and to Desika Narayanan for stimulating discussions. We also thank Padelis Papadopoulos for useful discussions and suggestions along the way. KPO gratefully acknowledge the support from the Lundbeck foundation and TRG acknowledges support from a STFC Advanced Fellowship. The Dark Cosmology Centre and Starplan are funded by the Danish National Research Foundation.

## REFERENCES

- Ackermann M., et al., 2013, *Science*, 339, 807  
 Adelberger K. L., Steidel C. C., Shapley A. E., Hunt M. P., Erb D. K., Reddy N. A., Pettini M., 2004, *ApJ*, 607, 226  
 Aravena M., et al., 2010, *ApJ*, 718, 177  
 Aravena M., et al., 2014, *MNRAS*, 442, 558  
 Asplund M., Grevesse N., Sauval A. J., Scott P., 2009, *ARA&A*, 47, 481  
 Bakes E. L. O., Tielens A. G. G. M., 1994, *ApJ*, 427, 822  
 Bigiel F., Leroy A., Walter F., Brinks E., de Blok W. J. G., Madore B., Thornley M. D., 2008, *AJ*, 136, 2846  
 Black J. H., Dalgarno A., 1977, *ApJs*, 34, 405  
 Blanc G. A., et al., 2013, *ApJ*, 764, 117  
 Blitz L., Rosolowsky E., 2006, *ApJ*, 650, 933  
 Blitz L., Fukui Y., Kawamura A., Leroy A., Mizuno N., Rosolowsky E., 2007, *Protostars and Planets V*, pp 81–96  
 Bolatto A. D., Leroy A. K., Rosolowsky E., Walter F., Blitz L., 2008, *ApJ*, 686, 948  
 Bovy J., Rix H.-W., Hogg D. W., 2012, *ApJ*, 751, 131  
 Brinch C., Hogerheijde M. R., 2010, *A&A*, 523, A25  
 Bryant P. M., Scoville N. Z., 1999, *AJ*, 117, 2632  
 Carilli C. L., Riechers D., Walter F., Maiolino R., Wagg J., Lentati L., McMahon R., Wolfe A., 2013, *ApJ*, 763, 120  
 Carroll T. J., Goldsmith P. F., 1981, *ApJ*, 245, 891  
 Cazaux S., Spaans M., 2004, *ApJ*, 611, 40  
 Chabrier G., 2003, *PASP*, 115, 763  
 Chapman S. C., et al., 2000, *MNRAS*, 319, 318  
 Christensen C., Quinn T., Governato F., Stilp A., Shen S., Wadsley J., 2012, *MNRAS*, 425, 3058  
 Daddi E., Cimatti A., Renzini A., Fontana A., Mignoli M., Pozzetti L., Tozzi P., Zamorani G., 2004, *ApJ*, 617, 746  
 Daddi E., et al., 2007, *ApJ*, 670, 156  
 Daddi E., et al., 2010, *ApJ*, 713, 686  
 Daddi E., et al., 2014, preprint, ([arXiv:1409.8158](https://arxiv.org/abs/1409.8158))  
 Dame T. M., Hartmann D., Thaddeus P., 2001, *ApJ*, 547, 792  
 Dannerbauer H., Daddi E., Riechers D. A., Walter F., Carilli C. L., Dickinson M., Elbaz D., Morrison G. E., 2009, *ApJL*, 698, L178  
 Downes D., Solomon P. M., 1998, *ApJ*, 507, 615  
 Draine B. T., 2011, *Physics of the Interstellar and Inter-galactic Medium*. Princeton University Press  
 Dumke M., 2000, in Alloin D., Olsen K., Galaz G., eds, *Astronomical Society of the Pacific Conference Series Vol. 221, Stars, Gas and Dust in Galaxies: Exploring the Links*. p. 15 ([arXiv:astro-ph/0012171](https://arxiv.org/abs/astro-ph/0012171))  
 Elbaz D., et al., 2007, *A&A*, 468, 33  
 Elmegreen B. G., 1989, *ApJ*, 344, 306  
 Fixsen D. J., Bennett C. L., Mather J. C., 1999, *ApJ*, 526, 207  
 Geach J. E., Papadopoulos P. P., 2012, *ApJ*, 757, 156  
 Genzel R., et al., 2013, *ApJ*, 773, 68  
 Gieles M., Portegies Zwart S. F., Baumgardt H., Athanassoula E., Lamers H. J. G. L. M., Sipior M., Leenaarts J., 2006, *MNRAS*, 371, 793  
 Glover S. C. O., Clark P. C., 2012, *MNRAS*, 421, 9  
 Goldsmith P. F., 2001, *ApJ*, 557, 736  
 Greve T. R., Sommer-Larsen J., 2008, *A&A*, 480, 335  
 Haardt F., Madau P., 2001, in Neumann D. M., Tran J. T. V., eds, *Clusters of Galaxies and the High Redshift Universe Observed in X-rays*. ([arXiv:astro-ph/0106018](https://arxiv.org/abs/astro-ph/0106018))

<sup>4</sup> <http://www.strw.leidenuniv.nl/~moldata/>, Schöier et al. (2005)

- Heiderman A., Evans II N. J., Allen L. E., Huard T., Heyer M., 2010, *ApJ*, 723, 1019
- Heyer M. H., Brunt C. M., 2004, *ApJL*, 615, L45
- Heyer M. H., Carpenter J. M., Snell R. L., 2001, *ApJ*, 551, 852
- Heyer M., Krawczyk C., Duval J., Jackson J. M., 2009, *ApJ*, 699, 1092
- Hodge J. A., Riechers D., Decarli R., Walter F., Carilli C. L., Daddi E., Dannerbauer H., 2014, preprint, ([arXiv:1412.2132](#))
- Iono D., et al., 2009, *ApJ*, 695, 1537
- Kauffmann J., Pillai T., Shetty R., Myers P. C., Goodman A. A., 2010, *ApJ*, 712, 1137
- Kennicutt Jr. R. C., 1998, *ARA&A*, 36, 189
- Krumholz M. R., Gnedin N. Y., 2011, *ApJ*, 729, 36
- Krumholz M. R., McKee C. F., Tumlinson J., 2009, *ApJ*, 699, 850
- Lagos C. d. P., Bayet E., Baugh C. M., Lacey C. G., Bell T. A., Fanidakis N., Geach J. E., 2012, *MNRAS*, 426, 2142
- Larson R. B., 1981, *MNRAS*, 194, 809
- Lee H.-H., Bettens R. P. A., Herbst E., 1996, *A&As*, 119, 111
- Leroy A. K., Walter F., Brinks E., Bigiel F., de Blok W. J. G., Madore B., Thornley M. D., 2008, *AJ*, 136, 2782
- Leroy A. K., et al., 2015, *ApJ*, 801, 25
- Magnelli B., et al., 2012, *A&A*, 548, A22
- Mao R.-Q., Schulz A., Henkel C., Mauersberger R., Muters D., Dinh-V-Trung 2010, *ApJ*, 724, 1336
- McMillan P. J., 2011, *MNRAS*, 414, 2446
- Miettinen O., Harju J., Haikala L. K., Kainulainen J., Johansson L. E. B., 2009, *A&A*, 500, 845
- Monaghan J. J., 2005, *Reports on Progress in Physics*, 68, 1703
- Muñoz J. A., Furlanetto S. R., 2014, *MNRAS*, 438, 2483
- Narayanan D., Hopkins P. F., 2013, *MNRAS*, 433, 1223
- Narayanan D., Krumholz M. R., 2014, *MNRAS*, 442, 1411
- Narayanan D., et al., 2006, *ApJL*, 642, L107
- Narayanan D., et al., 2008a, *ApJS*, 174, 13
- Narayanan D., et al., 2008b, *ApJs*, 176, 331
- Narayanan D., Cox T. J., Shirley Y., Davé R., Hernquist L., Walker C. K., 2008c, *ApJ*, 684, 996
- Narayanan D., Cox T. J., Hayward C. C., Younger J. D., Hernquist L., 2009, *MNRAS*, 400, 1919
- Narayanan D., Krumholz M., Ostriker E. C., Hernquist L., 2011, *MNRAS*, 418, 664
- Narayanan D., Krumholz M. R., Ostriker E. C., Hernquist L., 2012, *MNRAS*, 421, 3127
- Norman C. A., Spaans M., 1997, *ApJ*, 480, 145
- Obreschkow D., Klöckner H.-R., Heywood I., Levrier F., Rawlings S., 2009, *Apj*, 703, 1890
- Obreschkow D., Heywood I., Rawlings S., 2011, *ApJ*, 743, 84
- Padoan P., Nordlund Å., 2002, *ApJ*, 576, 870
- Papadopoulos P. P., Thi W.-F., 2013, in Torres D. F., Reimer O., eds, *Advances in Solid State Physics Vol. 34, Cosmic Rays in Star-Forming Environments*. p. 41 ([arXiv:1207.2048](#)), doi:10.1007/978-3-642-35410-6\_5
- Papadopoulos P. P., Isaak K., van der Werf P., 2010, *ApJ*, 711, 757
- Papadopoulos P. P., Thi W.-F., Miniati F., Viti S., 2011, *MNRAS*, 414, 1705
- Papadopoulos P. P., van der Werf P. P., Kılouris E. M., Isaak K. G., Gao Y., Mühle S., 2012, *MNRAS*, 426, 2601
- Papadopoulos P. P., et al., 2014, *ApJ*, 788, 153
- Papovich C., Finkelstein S. L., Ferguson H. C., Lotz J. M., Gialalisco M., 2011, *MNRAS*, 412, 1123
- Pelupessy F. I., 2005, PhD thesis, Leiden Observatory, Leiden University, P.O. Box 9513, 2300 RA Leiden, The Netherlands
- Pelupessy F. I., Papadopoulos P. P., van der Werf P., 2006, *ApJ*, 645, 1024
- Pineda J. E., Caselli P., Goodman A. A., 2008, *ApJ*, 679, 481
- Pineda J. L., Langer W. D., Velusamy T., Goldsmith P. F., 2013, *A&A*, 554, A103
- Popping G., Somerville R. S., Trager S. C., 2014, *MNRAS*, 442, 2398
- Price D. J., 2007, *Publications of the Astronomical Society of Australia*, 24, 159
- Puchwein E., Bolton J. S., Haehnelt M. G., Madau P., Becker G. D., 2014, preprint, ([arXiv:1410.1531](#))
- Rodighiero G., et al., 2010, *A&A*, 518, L25
- Röllig M., Ossenkopf V., Jeyakumar S., Stutzki J., Sternberg A., 2006, *A&A*, 451, 917
- Romeo A. D., Sommer-Larsen J., Portinari L., Antonuccio-Delogu V., 2006, *MNRAS*, 371, 548
- Saintonge A., et al., 2011, *MNRAS*, 415, 32
- Sandstrom K. M., et al., 2013, *ApJ*, 777, 5
- Schöier F. L., van der Tak F. F. S., van Dishoeck E. F., Black J. H., 2005, *A&A*, 432, 369
- Seon K.-I., et al., 2011, *ApJs*, 196, 15
- Simnett G. M., McDonald F. B., 1969, *ApJ*, 157, 1435
- Smith R. J., Glover S. C. O., Clark P. C., Klessen R. S., Springel V., 2014, *MNRAS*, 441, 1628
- Sofia U. J., Lauroesch J. T., Meyer D. M., Cartledge S. I. B., 2004, *ApJ*, 605, 272
- Solomon P. M., Downes D., Radford S. J. E., Barrett J. W., 1997, *ApJ*, 478, 144
- Sommer-Larsen J., Vedel H., Hellsten U., 1998, *MNRAS*, 294, 485
- Sommer-Larsen J., Götz M., Portinari L., 2003, *ApJ*, 596, 47
- Sommer-Larsen J., Romeo A. D., Portinari L., 2005, *MNRAS*, 357, 478
- Springel V., Hernquist L., 2003, *MNRAS*, 339, 289
- Stahler S. W., Palla F., 2005, *The Formation of Stars*. Wiley
- Stinson G., Seth A., Katz N., Wadsley J., Governato F., Quinn T., 2006, *MNRAS*, 373, 1074
- Strong A. W., Mattox J. R., 1996, *A&A*, 308, L21
- Swinbank A. M., et al., 2011, *ApJ*, 742, 11
- Tacconi L. J., et al., 2008, *ApJ*, 680, 246
- Tacconi L. J., et al., 2013, *ApJ*, 768, 74
- Tielens A. G. G. M., 2005, *The Physics and Chemistry of the Interstellar Medium*. Cambridge University Press
- Vázquez-Semadeni E., Colín P., Gómez G. C., Ballesteros-Paredes J., Watson A. W., 2010, *ApJ*, 715, 1302
- Webber W. R., 1998, *ApJ*, 506, 329
- Whitaker K. E., et al., 2011, *ApJ*, 735, 86
- Wiersma R. P. C., Schaye J., Smith B. D., 2009, *MNRAS*, 393, 99
- Wolfire M. G., McKee C. F., Hollenbach D., Tielens A. G. G. M., 2003, *ApJ*, 587, 278

- Wolfire M. G., Hollenbach D., McKee C. F., 2010, *ApJ*, 716, 1191  
 Yang B., Stancil P. C., Balakrishnan N., Forrey R. C., 2010, *ApJ*, 718, 1062  
 Zahid H. J., Dima G. I., Kewley L. J., Erb D. K., Davé R., 2012, *ApJ*, 757, 54

## APPENDIX A: THERMAL BALANCE OF THE ATOMIC GAS PHASE

As explained in § 3.2, we cool the initial hot SPH gas down by considering the following heating and cooling mechanisms and equating their energy rates:  $\Gamma_{\text{CR,H I}} = \Lambda_{\text{atoms+ions}} + \Lambda_{\text{rec}} + \Lambda_{\text{f-f}}$ .

$\Gamma_{\text{CR,H I}}$  is the heating rate of the atomic gas due to cosmic ray ionizations (Draine 2011):

$$\Gamma_{\text{CR,H I}} = 1.03 \times 10^{-27} n_{\text{H I}} \left( \frac{\zeta_{\text{CR,H I}}}{10^{-16}} \right) \times \left[ 1 + 4.06 \left( \frac{x_e}{x_e + 0.07} \right)^{1/2} \right] \text{ erg cm}^{-3} \text{ s}^{-1}, \quad (\text{A1})$$

where  $\zeta_{\text{CR,H I}}$  is the primary CR ionization rate of H I atoms (determined locally in our simulations according to eq. 12), and  $x_e$  is the hydrogen ionization fraction calculated with a procedure kindly provided by I. Pelupessy; see also Pelupessy (2005). The term containing  $x_e$  in eq. ?? accounts for the fact that in gas of high ionization, the electron created by the primary CR ionization has a high probability of transferring its kinetic energy into heat via long-range Coulomb scattering off free electrons. In the case of low ionization, this term becomes insignificant as a higher fraction of its energy will go to secondary ionizations or excitation of bound states in stead of heating.

$\Lambda_{\text{atoms+ions}}$  is the total cooling rate due line emission from H, He, C, N, O, Ne, Mg, Si, S, Ca, and Fe, calculated using the publically available code of Wiersma et al. (2009) which takes  $T_k$ ,  $n_{\text{H}}$  and the abundances of the above elements as input. Wiersma et al. (2009) compute the cooling rates with the photoionization package CLOUDY assuming CIE. They also adopt a value for the meta-galactic UV and X-ray field equal to that expected at  $z \sim 2$  (Haardt & Madau 2001). At  $z \sim 2$ , the emission rate of H I ionizing radiation is higher by a factor of about  $\sim 30$  than at  $z = 0$  (Puchwein et al. 2014), and thus plays an important role in metal line cooling calculations.

$\Lambda_{\text{rec}}$  is the cooling rate due to hydrogen recombination emission (Draine 2011):

$$\Lambda_{\text{rec}} = \alpha_B n_e n_{\text{H}} \langle E_{rr} \rangle \text{ ergs cm}^{-3} \text{ s}^{-1}, \quad (\text{A2})$$

where  $\alpha_B$  is the radiative recombination rate for hydrogen in the case of optically thick gas in which ionizing photons emitted during recombination are immediately reabsorbed. We adopt the approximation for  $\alpha_B$  given by Draine (2011):

$$\alpha_B = 2.54 \times 10^{-13} T_4^{(-0.8163 - 0.0208 \ln T_4)} \text{ cm}^3 \text{ s}^{-1}, \quad (\text{A3})$$

where  $T_4$  is defined as  $T_k/10^4 \text{ K}$ . The density of ionised hydrogen,  $n_{\text{H}^+}$ , is set equal to the electron density,  $n_e$ , and  $E_{rr}$  is the corresponding mean kinetic energy of the recombining electrons:

$$\langle E_{rr} \rangle = [0.684 - 0.0416 \ln T_4] k_B T_k \text{ ergs}. \quad (\text{A4})$$

$\Lambda_{\text{f-f}}$  is the cooling rate due to free-free emission from electrons in a pure H plasma (i.e., free electrons scattering off  $\text{H}^+$ ), and is given by (Draine 2011):

$$\Lambda_{\text{f-f}} = 0.54 T_4^{0.37} k_B T_k n_e n_{\text{H}^+} \alpha_B \text{ ergs cm}^{-3} \text{ s}^{-1}, \quad (\text{A5})$$

where the recombination rate,  $\alpha_B$ , is calculated in the same way as for  $\Lambda_{\text{rec}}$ .

Figure A1 shows the above heating and cooling rates pertaining to two example SPH particles with similar initial temperatures ( $\sim 10^4 \text{ K}$ ). Because of different ambient conditions (i.e.,  $n_{\text{H I}}$ ,  $x_e$ ,  $Z'$ , and  $\zeta_{\text{CR}}$ ) the equilibrium temperature solutions for the two gas particles end up being significantly different.

## APPENDIX B: THERMAL BALANCE OF THE MOLECULAR GAS PHASE

As described in Section 3.4 **S $\dot{\text{T}}$ GAME** assumes the molecular gas resides exclusively in giant molecular clouds that have Plummer radial density profiles (i.e., given by eq. 11). Throughout the clouds the gas temperature is solved for according to the heating and cooling equilibrium requirement  $\Gamma_{\text{PE}} + \Gamma_{\text{CR,H}_2} = \Lambda_{\text{H}_2} + \Lambda_{\text{CO}} + \Lambda_{\text{C II}} + \Lambda_{\text{O I}} + \Lambda_{\text{gas-dust}}$  (eq. 14).

$\Gamma_{\text{PE}}$  is the heating rate of the gas due to photo-electric ejection of electrons from dust grains by FUV photons, and is given by (Bakes & Tielens 1994):

$$\Gamma_{\text{PE}} = 10^{-24} \epsilon G'_{0,\text{att}} n_{\text{H}} \text{ ergs cm}^{-3} \text{ s}^{-1}, \quad (\text{B1})$$

where  $G'_{0,\text{att}}$  is the local attenuated FUV field in Habing units, derived following eq. 13, and  $\epsilon$  is the heating efficiency:

$$\epsilon = \frac{4.87 \times 10^{-2}}{1 + 4 \times 10^{-3} (G'_{0,\text{att}} T^{0.5} / n_e)^{0.73}} + \frac{3.65 \times 10^{-2}}{1 + 4 \times 10^{-3} (G'_{0,\text{att}} T^{0.5} / n_e)^{0.73}}, \quad (\text{B2})$$

where  $n_e$  is the electron density, calculated as  $x_e n_{\text{H}}$ , with  $x_e$  again calculated using the procedure of I. Pelupessy.

$\Gamma_{\text{CR,H}_2}$  is the heating rate by cosmic rays traveling through molecular gas (Stahler & Palla 2005):

$$\Gamma_{\text{CR,H}_2} = 1.068 \times 10^{-24} \left( \frac{\zeta_{\text{CR,H}_2}}{10^{-16}} \right) \left( \frac{n_{\text{H}_2}}{10^3 \text{ cm}^{-3}} \right) \text{ ergs cm}^{-3} \text{ s}^{-1} \quad (\text{B3})$$

where  $\zeta_{\text{CR,H}_2}$  is the local CR primary ionization rate of  $\text{H}_2$  molecules, which is approximately  $1.6\times$  higher than of H I atoms (Stahler & Palla 2005).

$\Lambda_{\text{H}_2}$  is the  $\text{H}_2$  line cooling rate, and we use the parameterization made by Papadopoulos et al. (2014) that includes the two lowest  $\text{H}_2$  rotational lines (S(0) and S(1), the only lines excited for  $T_k \lesssim 1000 \text{ K}$ ):

$$\Lambda_{\text{H}_2} = 2.06 \times 10^{-24} \frac{n_{\text{H}_2}}{1 + r_{\text{op}}} \left[ 1 + \frac{1}{5} e^{510 \text{ K} / T_k} \left( 1 + \frac{n_0}{n_{\text{H}_2}} \right) \right]^{-1} \times (1 + R_{10}) \text{ ergs cm}^{-3} \text{ s}^{-1}, \quad (\text{B4})$$

where  $R_{10}$  is defined as:

$$R_{10} = 26.8 r_{\text{op}} \left[ \frac{1 + (1/5) e^{510 \text{ K} / T_k} \left( 1 + \frac{n_0}{n_{\text{H}_2}} \right)}{1 + (3/7) e^{845 \text{ K} / T_k} \left( 1 + \frac{n_1}{n_{\text{H}_2}} \right)} \right], \quad (\text{B5})$$



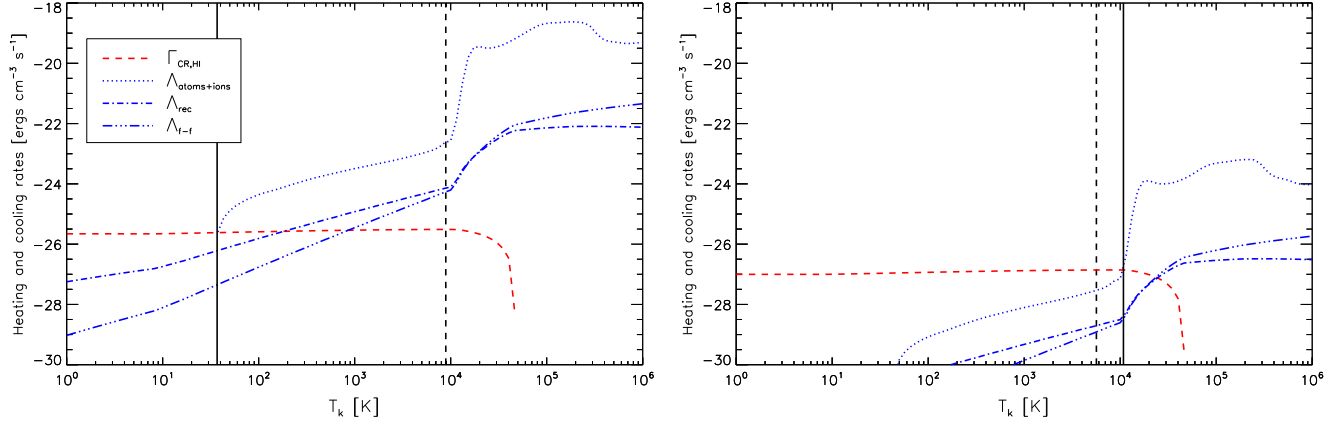


**Figure A1.** Heating and cooling rates as functions of temperature for two SPH gas particles with  $[n_{\text{H}} = 14.62 \text{ cm}^{-3}, \zeta_{\text{CR}} = 4.02 \times 10^{-16} \text{ s}^{-1}, x_{\text{e}} (T_{\text{k,SPH}} = 8892 \text{ K}) = 0.006]$  (left) and  $[n_{\text{H}} = 0.09 \text{ cm}^{-3}, \zeta_{\text{CR}} = 3.92 \times 10^{-16} \text{ s}^{-1}, x_{\text{e}} (T_{\text{k,SPH}} = 5649 \text{ K}) = 0.001]$  (right). The left-hand side plot illustrates the case of an SPH particle of high gas density and metallicity leading to relatively high metal line cooling as compared to the heating from cosmic rays of moderate intensity. This results in a low temperature for the WCNM of  $T_{\text{k}} = 37 \text{ K}$ . The right-hand side plot shows a case of lower density and metallicity causing less cooling by metal lines, hence a higher equilibrium temperature for a similar cosmic ray field strength. Vertical black solid lines mark the resulting temperature of the neutral gas phase in each SPH particle, found where the difference between heating and cooling rate is smallest, when starting at the original SPH gas temperature, indicated with vertical black dashed lines.

and  $n_0 \sim 54 \text{ cm}^{-3}$  and  $n_1 \sim 10^3 \text{ cm}^{-3}$  are the critical densities of the S(0):2-0 and S(1):3-1 rotational lines.  $r_{\text{op}}$  is the ortho- $\text{H}_2$ /para- $\text{H}_2$  ratio (set to 3 which is the equilibrium value).

For the cooling rates due to the  $[\text{C II}]158 \mu\text{m}$  and  $[\text{O I}]63 \mu\text{m} + 146 \mu\text{m}$  fine-structure lines we adopt the parameterizations by Röllig et al. (2006). The C II cooling rate ( $\Lambda_{\text{C II}}$ ) is:

$$\Lambda_{\text{C II}} = 2.02 \times 10^{-24} n_{\text{Z}'} \quad (\text{B6})$$

$$\times \left[ 1 + \frac{1}{2} e^{92\text{K}/T_{\text{k}}} (1 + 1300/n_{\text{H}}) \right]^{-1} \text{ ergs cm}^{-3} \text{ s}^{-1},$$

where a carbon to hydrogen abundance ratio that scales with metallicity according to  $\chi_{[\text{C}]} = 1.4 \times 10^{-4} Z'$  is assumed. For the parameterization of the O I cooling rate ( $\Lambda_{\text{O I}} = \Lambda_{63\mu\text{m}} + \Lambda_{146\mu\text{m}}$ ) we refer to eqs. A.5 and A.6 in Röllig et al. (2006) and simply note that we adopt (in accordance with Röllig et al. (2006)) an oxygen to hydrogen abundance ratio of  $\chi_{[\text{O}]} = 3 \times 10^{-4} Z'$ .

$\Lambda_{\text{CO}}$  is the cooling rate due to CO rotational transitions. We use the parameterization provided by Papadopoulos & Thi (2013):

$$\Lambda_{\text{CO}} = 4.4 \times 10^{-24} \left( \frac{n_{\text{H}_2}}{10^4} \right)^{3/2} \left( \frac{T_{\text{k}}}{10 \text{ K}} \right)^2 \left( \frac{\chi_{\text{CO}}}{\chi_{[\text{C}]}} \right) \text{ ergs cm}^{-3} \text{ s}^{-1}, \quad (\text{B7})$$

where  $\chi_{\text{CO}}/\chi_{[\text{C}]}$  is the relative CO to neutral carbon abundance ratio, the value of which we determine by interpolation, assuming that  $\chi_{\text{CO}}/\chi_{[\text{C}]} = (0.97, 0.98, 0.99, 1.0)$  for  $n_{\text{H}_2} = 5 \times 10^3, 10^4, 10^5, 10^6 \text{ cm}^{-3}$ , respectively (Papadopoulos & Thi 2013).

$\Lambda_{\text{gas-dust}}$  is the cooling rate due to gas-dust interactions and is given by (Papadopoulos et al. 2011):

$$\Lambda_{\text{gas-dust}} = 3.47 \times 10^{-33} n_{\text{H}}^2 \sqrt{T_{\text{k}}} (T_{\text{k}} - T_{\text{dust}}) \text{ ergs cm}^{-3} \text{ s}^{-1}, \quad (\text{B8})$$

where the dust temperature ( $T_{\text{dust}}$ ) is calculated using eq. 15 (Section 3.4.3).

## APPENDIX C: GMC MODELS

Each SPH particle is divided into several GMCs as described in § 3.4.1, and we derive the molecular gas density and temperature within each from three basic parameters which are SFR density, GMC mass,  $m_{\text{GMC}}$ , and metallicity,  $Z'/Z_{\odot}$ . Derived from these basic parameters are the far-UV and cosmic ray field strengths, the  $\text{H}_2$  gas mass fraction of each SPH particles, as well as the GMC properties used to derive the CO excitation and emission;  $\text{H}_2$  density and temperature. Histograms of the basic parameters are shown in Figure C1, while properties derived thereof can be found in Figure C2.

This paper has been typeset from a  $\text{T}_{\text{E}}\text{X}/\text{L}^{\text{A}}\text{T}_{\text{E}}\text{X}$  file prepared by the author.

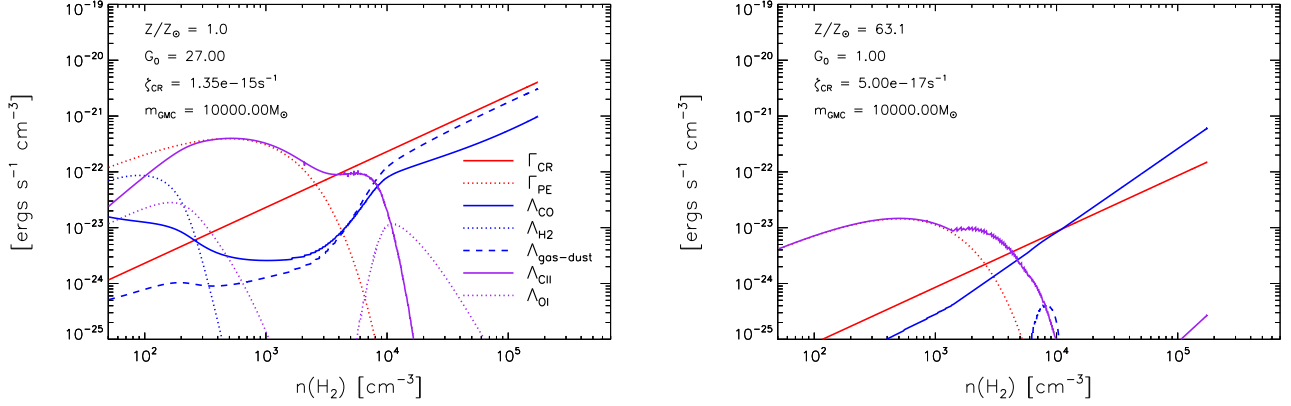


**Figure B1.** Equilibrium heating (red curves) and cooling (blue+purple curves) rates as functions of  $\text{H}_2$  density for two different GMC models with  $[m_{\text{GMC}} = 10^4 M_{\odot}, Z' = 1, G'_0 = 27, P_{\text{ext}} = 10^4 \text{ K cm}^{-3}]$  (left) and  $[m_{\text{GMC}} = 10^4 M_{\odot}, Z' = 63, G'_0 = 1, P_{\text{ext}} = 10^4 \text{ K cm}^{-3}]$  (right). In the case of high FUV and cosmic ray fields (left), heating and cooling in the outer region ( $n_{\text{H}_2} \lesssim 1500 \text{ cm}^{-3}$ ) are dominated by photoelectric heating (red dotted) and  $[\text{CII}]$  line cooling (purple solid), while in the inner region ( $n_{\text{H}_2} \gtrsim 10000 \text{ cm}^{-3}$ ), cosmic ray heating (red solid) and gas-dust interactions (blue dashed) are the important mechanisms in determining the temperature. In the case of high metallicity (right), photoelectric heating and  $[\text{CII}]$  line cooling are also dominating in the outer region, but cooling in the inner region is mainly controlled by CO line emission.

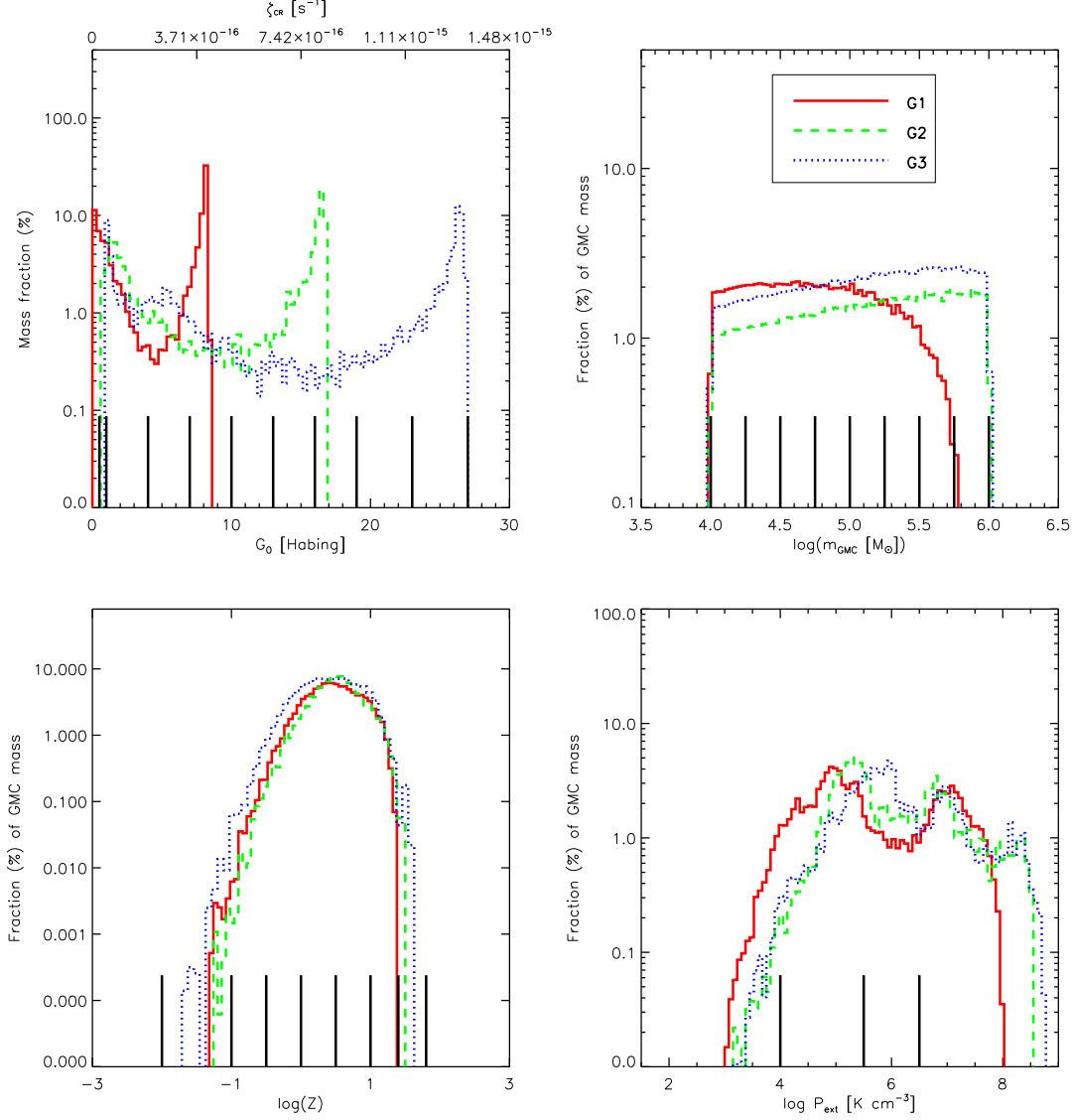


**Figure C1.** Mass-weighted histograms of the basic parameters of the GMCs in G1 (red solid), G2 (green dashed), and G3 (blue dotted). From top left and clockwise: the local far-UV field ( $G'_0$ ) (and CR ionization rate since  $\zeta_{\text{CR}} \propto G'_0$ ), GMC mass ( $m_{\text{GMC}}$ ), metallicity ( $Z'$ ) and external pressure ( $P_{\text{ext}}$ ). Black vertical lines indicate the  $G'_0$ ,  $m_{\text{GMC}}$ ,  $Z'$ ,  $P_{\text{ext}}$ -values for which  $T_{\text{k}} - n_{\text{H}_2}$  curves were calculated (see Figure C2) – a total of 630 GMCs which make up our grid GMC models. Each GMC in the galaxies is assigned the  $T_{\text{k}} - n_{\text{H}_2}$  curve of the GMC model at the closest grid point.

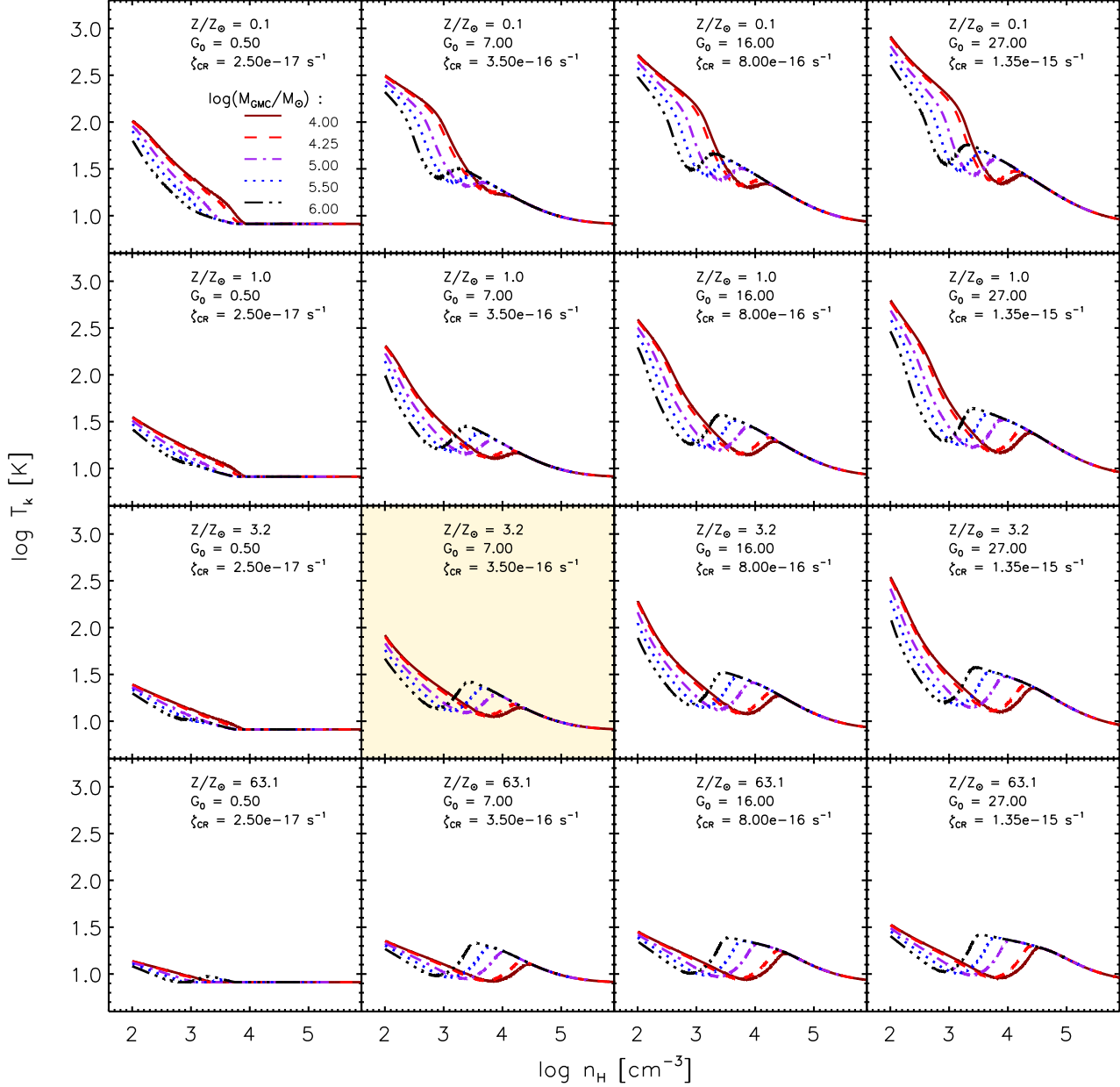


**Figure C2.** Kinetic temperature versus  $\text{H}_2$  density curves for 80 out of the 630 grid model GMCs that span the full ( $G'_0$ ,  $M_{\text{GMC}}$ ,  $Z'$ ) parameter space set by and marked on top of the distributions in Figure C1 (see also Section 3.4.4) for a pressure of  $P_{\text{ext}} = 10^4 \text{ K cm}^{-3}$ . The grid model most often assigned to GMCs in G1 is indicated by the red dashed curve in the highlighted panel and corresponds to  $G'_0 = 7.0$  ( $\zeta_{\text{CR}} = 3.5 \times 10^{-16} \text{ s}^{-1}$ ),  $\log m_{\text{GMC}}/M_{\odot} = 4.25$ , and  $Z' = 3.2$ . In general, higher metallicity (from top to bottom) leads to more cooling via emission lines of ions, atoms and molecules, and hence lower temperatures. On the other hand, higher UV and CR fields (from left to right) cause more heating and therefore higher  $T_k$ . The decreasing trend of  $T_k$  with higher values of  $n_{\text{H}_2}$  is mainly caused by the gradual attenuation of the UV field as one moves into the cloud. The ‘bump’ at  $n_{\text{H}_2} \sim 10^3 - 10^4 \text{ cm}^{-3}$  corresponds to the transition from CII line cooling to the less efficient CO line cooling at higher densities. At densities above  $n_{\text{H}_2} = 10^4 \text{ cm}^{-3}$ , gas-dust interactions set in and eventually cools the gas down to the CMB temperature in all GMC cores.

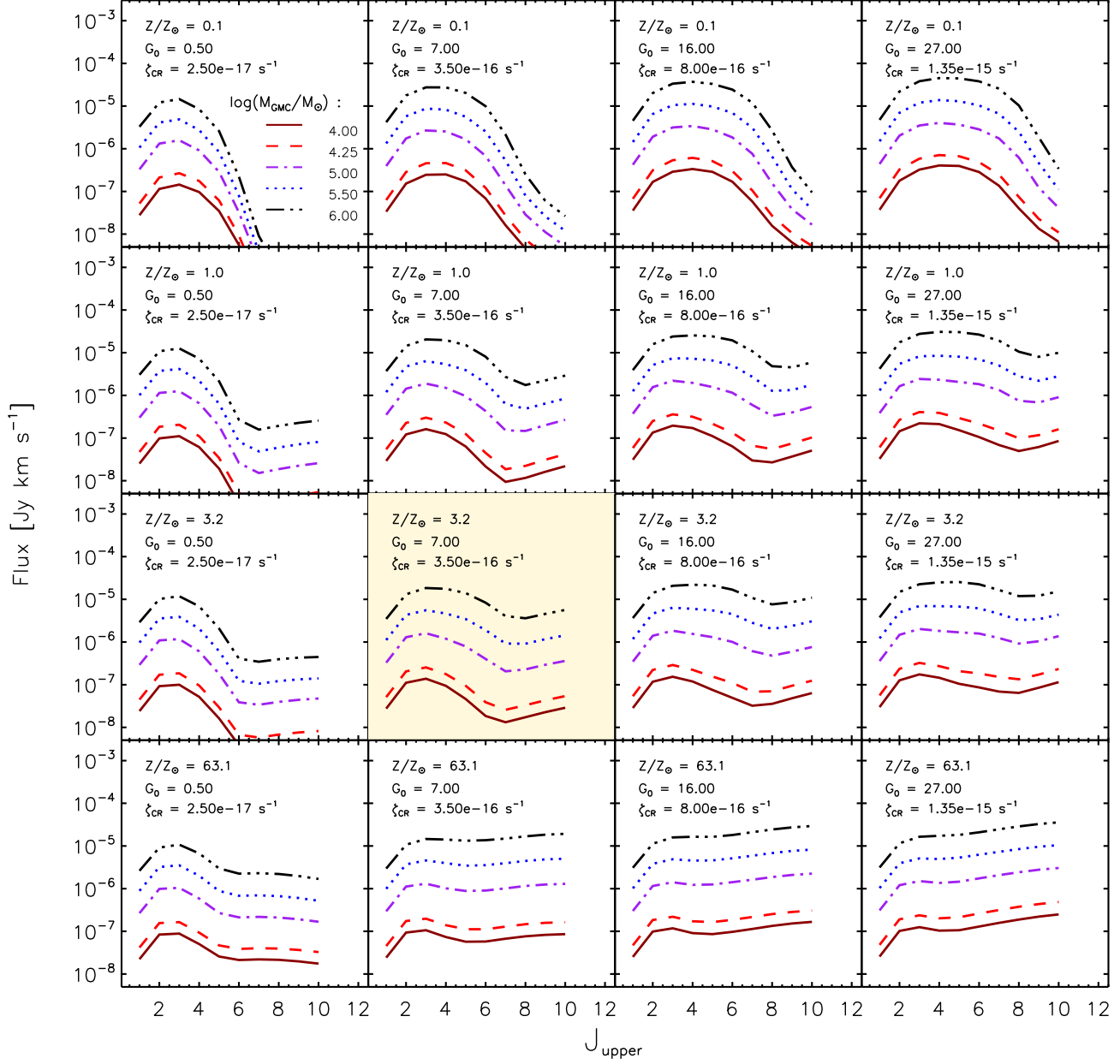


**Figure C3.** CO SLEDs obtained with LIME for the 80 model GMCs whose  $T_{\text{k}} - n_{\text{H}_2}$  curves are shown in Figure C2. The CO SLED used most often in G1 is shown as the red dashed curve in the highlighted panel. These CO SLEDs were made for a fixed external pressure of  $P_{\text{ext}}/k_{\text{B}} = 10^4 \text{ cm}^{-3} \text{ K}$  and a default Plummer density profile.

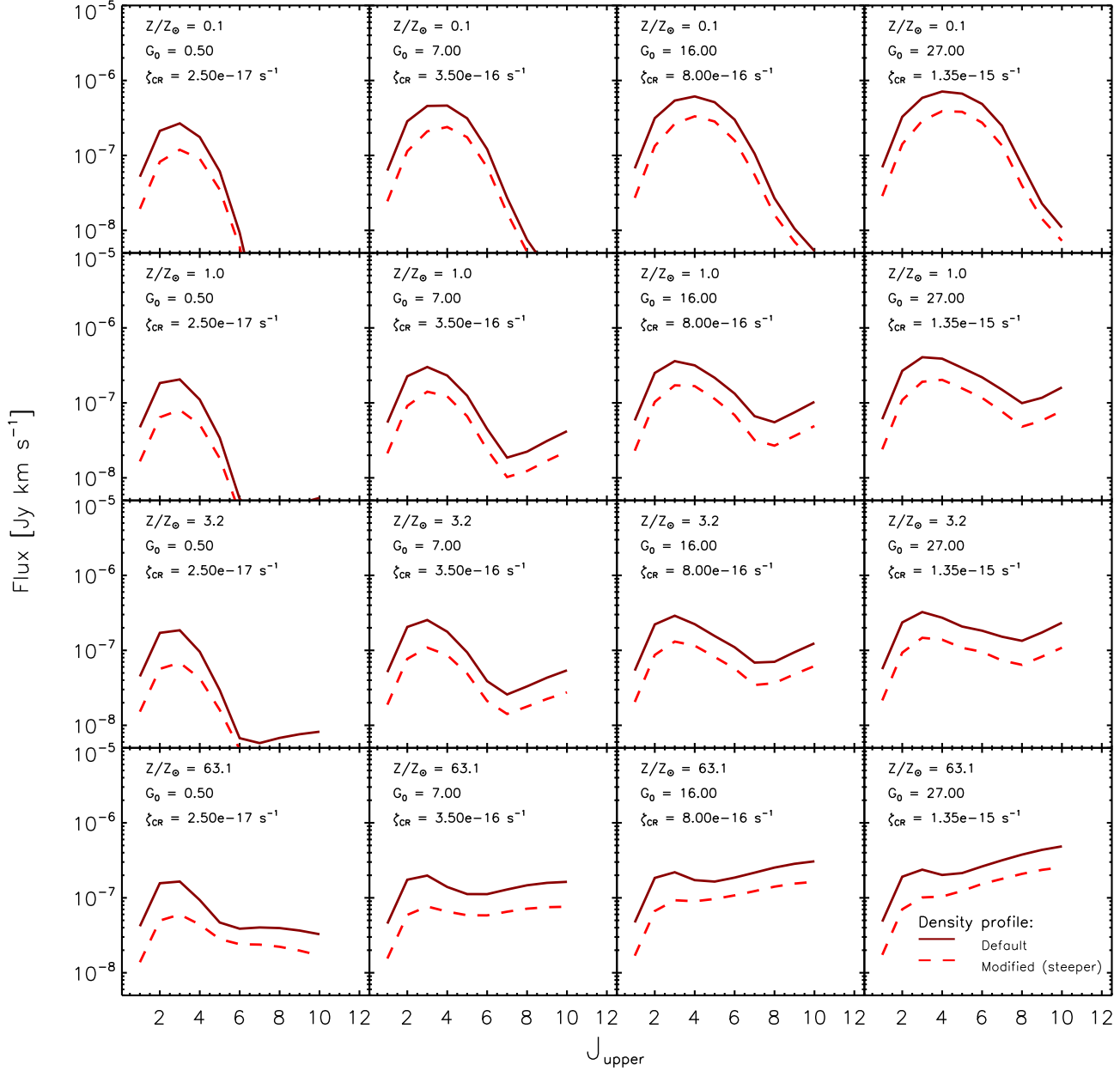


**Figure C4.** CO SLEDs obtained with LIME for the same  $[G'_0, Z']$  values as shown in the panels of Figure C3 for Plummer density profiles with power-law index  $-5/2$  (solid curve) and  $-7/2$  (dashed curve). In all panels, the external pressure has been fixed to  $P_{\text{ext}}/k_B = 10^4 \text{ cm}^{-3} \text{ K}$  and the GMC mass to  $m_{\text{GMC}} = 10^{4.25} M_{\odot}$ .

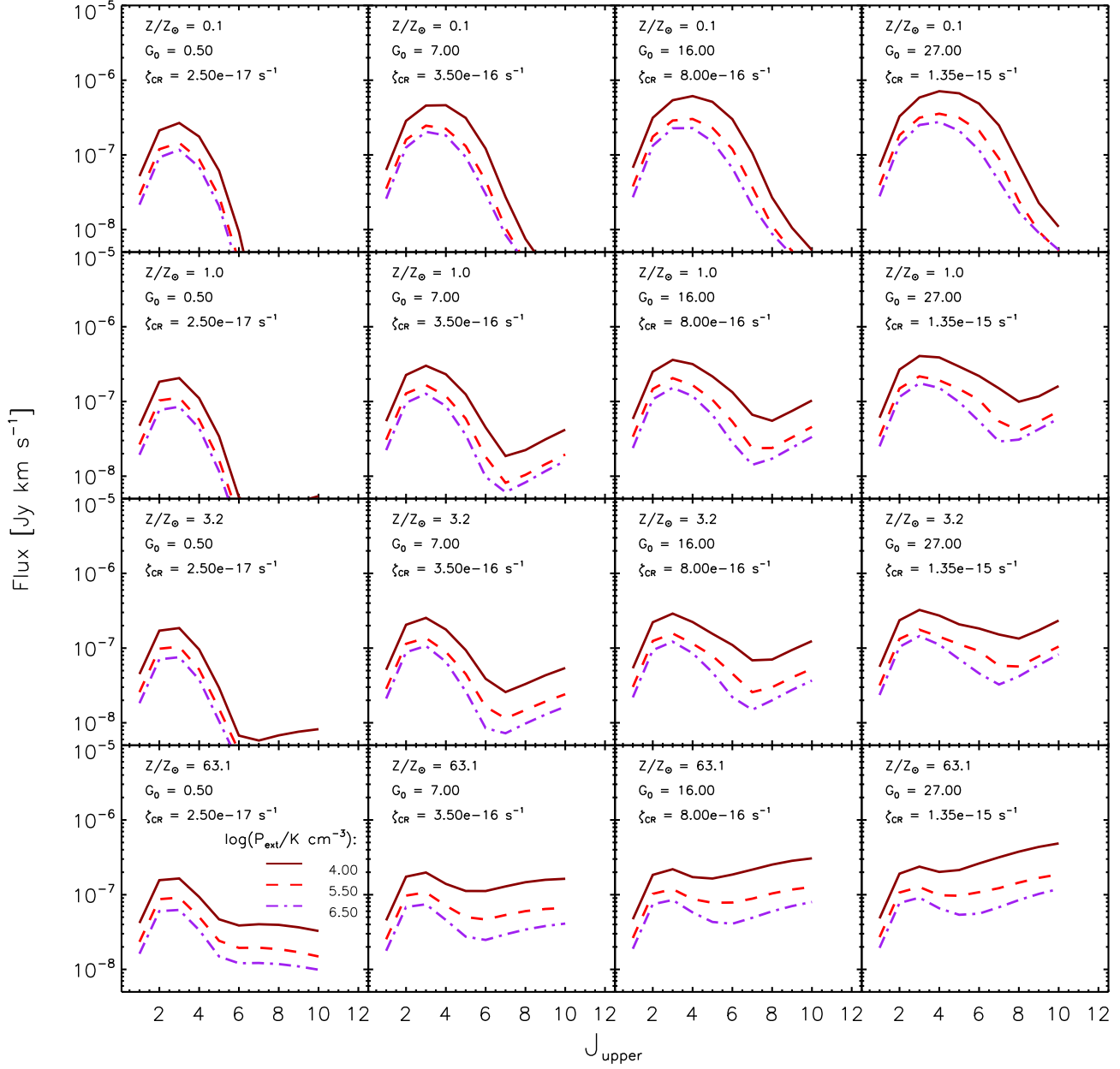


**Figure C5.** CO SLEDs obtained with LIME for the same  $[G'_0, Z']$  values as shown in the panels of Figure C3 for  $P_{\text{ext}}/k_B = 10^4 \text{ cm}^{-3} \text{ K}$  (solid curves),  $10^{5.5} \text{ cm}^{-3} \text{ K}$  (dashed curves), and  $10^{6.5} \text{ cm}^{-3} \text{ K}$  (dot-dashed curves). In all panels, the GMC mass is fixed to  $10^{4.25} M_\odot$ . Higher pressure environments are seen to lead to a decrease in luminosity for all transitions.